225 (2023) 211701

Contents lists available at ScienceDirect

Geoenergy Science and Engineering

journal homepage: www.sciencedirect.com/journal/geoenergy-science-and-engineering

Reservoir characteristics of different shale lithofacies and their effects on the gas content of Wufeng-Longmaxi Formation, southern Sichuan Basin, China

Chao Qian [a,b,c,*], Xizhe Li [b,**], Qing Zhang [a], Weijun Shen [c,***], Wei Guo [b], Wei Lin [d], Lingling Han [b,e], Yue Cui [b,e], Yize Huang [b,e], Xiangyang Pei [b], Zhichao Yu [f]

[a] Shale Gas Exploration and Development Department, CNPC Chuanqing Drilling Engineering Co., Ltd., Chengdu, Sichuan, 610051, China
[b] Research Institute of Petroleum Exploration and Development, PetroChina, Beijing, 100083, China
[c] Key Laboratory for Mechanics in Fluid Solid Coupling Systems, Institute of Mechanics, Chinese Academy of Sciences, Beijing, 100190, China
[d] School of Geosciences, Yangtze University, Wuhan, 430100, China
[e] Institute of Porous Flow and Fluid Mechanics, Chinese Academy of Sciences, Langfang, Hebei, 065007, China
[f] College of Geosciences, China University of Petroleum, Beijing, 102249, China

ARTICLE INFO

Keywords:
Shale lithofacies
Pore structure characteristics
Water saturation
High-pressure methane adsorption
Gas content
Wufeng-Longmaxi Formation

ABSTRACT

Various shale lithofacies differ significantly in terms of gas content and pore structure characteristics. In this study, FE-SEM, low-pressure gas adsorption (LPGA), in-situ reservoir water saturation restoring, and high-pressure (0–51Mpa) methane adsorption were conducted to systematically characterize pore structure and evaluate the gas content of different shale lithofacies in the Wufeng-Longmaxi Formation, southern Sichuan Basin. The mineral compositions identified four shale lithofacies, and pores are abundant in siliceous shale and mixed shale. Siliceous shale has the largest pore volume (PV) and specific surface area (SSA), averaging 0.0310 cm^3/g and 25.827 m^2/g, respectively. However, the PV and SSA are lowest in argillaceous shale, averaging 0.0217 cm^3/g and 18.734 m^2/g, respectively. Water saturation is positively correlated with clay minerals, and argillaceous shale possess the highest water saturation of 60% due to the highest clay content. The supercritical Dubinin-Astakhov (S-DA) excess adsorption model predictions deviated less from the measured data and fitted well. The shale adsorption capacity are dominated by TOC content and total SSA. However, water and temperature have an inhibitory activity on adsorption capacity, with the adsorption capacity of water-bearing shales decreasing by 28%~81% at a water saturation of 30%~65% compared to dry shales. As the temperature increased from 40 °C to 80 °C, the methane adsorption capacity decreased from 3.95 to 2.79 m^3/t, a 29% decrease. The shale gas content prediction models were established and extrapolated into the functions of reservoir depth. Deep shale gas reservoirs are dominated by free gas, accounting for over 90% at 5000 m. Siliceous shale has the highest gas content, followed by mixed shale, argillaceous-siliceous shale, and argillaceous shale. It is estimated that siliceous shale has a three-fold higher gas content than argillaceous shale. Siliceous and mixed shale are favorable reservoirs for shale gas exploration and development due to their high gas contents and low water saturation.

1. Introduction

In China, shale gas is becoming crucial to meeting the demand for economic and social development. Due to the extremely low permeability of shale reservoirs, shale gas fields have only been successfully developed with horizontal drilling and hydraulic fracturing techniques

* Corresponding author. Shale Gas Exploration and Development Department, CNPC Chuanqing Drilling Engineering Co., Ltd., Chengdu, Sichuan, 610051, China.
** Corresponding author.
*** Corresponding author.
E-mail addresses: chaoqian19@outlook.com (C. Qian), lxz69@petrochina.com.cn (X. Li), zhangq_ccde@cnpc.com.cn (Q. Zhang), wjshen763@imech.ac.cn (W. Shen), pkuguowei69@petrochina.com.cn (W. Guo), ucaslinwei@126.com (W. Lin), hanll_19@163.com (L. Han), yueyuxinfei1995@163.com (Y. Cui), huangyize20@mails.ucas.ac.cn (Y. Huang), xiangyangpei328@163.com (X. Pei), 18627223527@126.com (Z. Yu).

https://doi.org/10.1016/j.geoen.2023.211701
Received 23 June 2022; Received in revised form 9 February 2023; Accepted 16 March 2023
Available online 17 March 2023

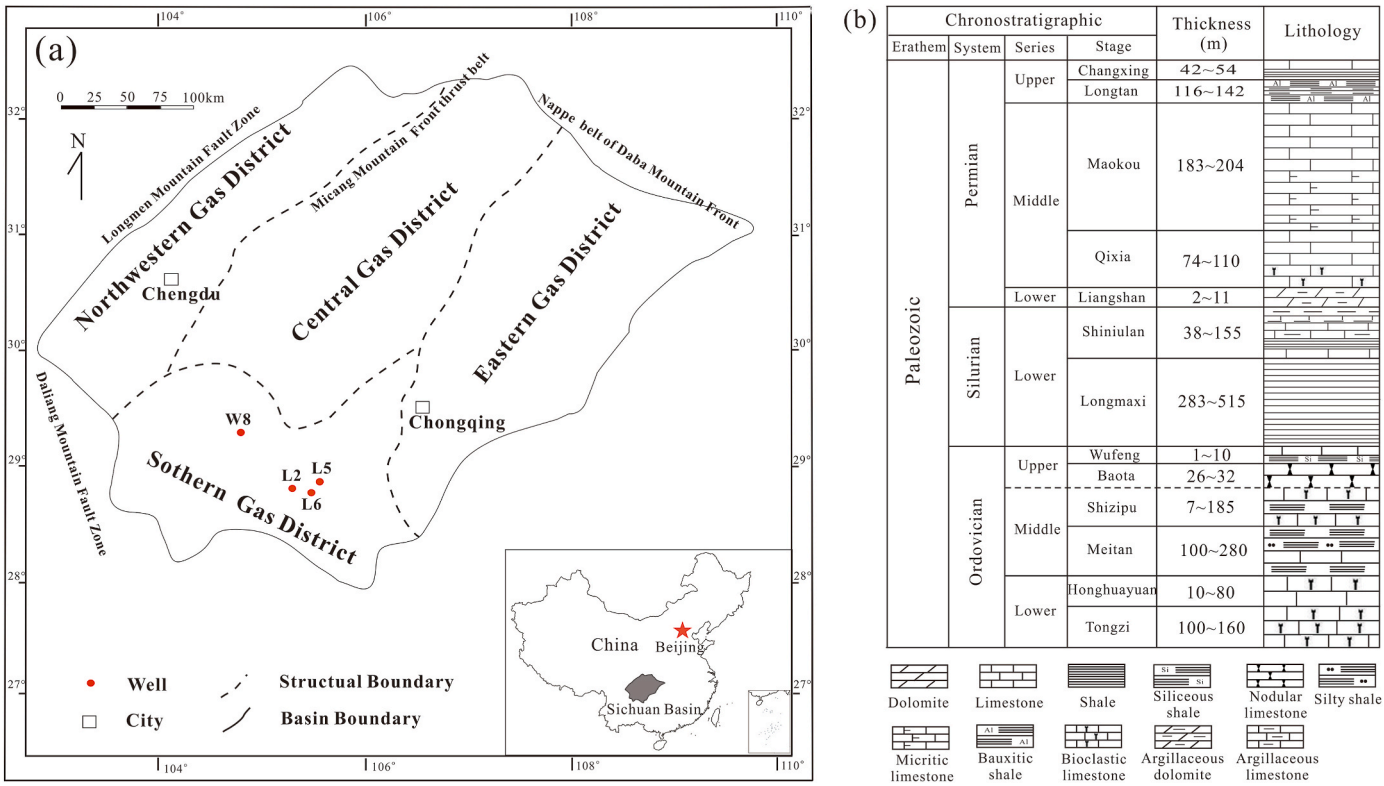

Fig. 1. Study area location and stratigraphic units of the southern Sichuan Basin.

over the past few decades (Hughes, 2013; Shen et al., 2022). Shale gas production in China reached 230×10^8 m^3 in 2021, growing at an annual rate of over 30×10^8 m^3, making it the world's second largest producer. Shale gas reserves and future production enhancement will be derived from the marine shale in Sichuan Basin (Ma et al., 2020; Han et al., 2022). As exploration and development progress, it is noted that significant differences in wells productions depend on their lithofacies (Gou et al., 2020; Xu et al., 2020a). A lithofacies combines mineral composition, texture, rock color, layering and grain size, etc. (Loucks and Ruppel, 2007; Yang et al., 2019; Pan et al., 2020). Lithofacies consisted of different mineral compositions, TOC, and the shale pores system varies largely from one formation to another (Tang et al., 2016; Wang et al., 2017; Zhang et al., 2018; Xu et al., 2020a). Shale gas is mainly adsorbed on pore surfaces as adsorbed gas, while free gas molecules exist in pore and microfracture spaces (Curtis, 2002; Ambrose et al., 2012; Qi et al., 2017; Chen et al., 2019). Thus, a comprehensive understanding of the pore structure of shale is essential for estimating shale gas reserves and gas content. The FE-SEM allows the morphology and size of nanoscale pores to be observed directly (Loucks et al., 2009; Yang et al., 2016; Lin et al., 2018; Chandra and Vishal, 2021). By using the FE-SEM image stitching technique, the pores and microfractures of the shale samples can be extracted and analysed (Li et al., 2021; Qian et al., 2022). Additionally, low-pressure gas adsorption (LPGA), and low field NMR, can reveal pore volume (PV), specific surface area (SSA), and pore size distributions (PSD) from nanometres to millimeters (Clarkson et al., 2013; Mastalerz et al., 2013; Zhang et al., 2017).

The adsorbed gas of shale gas reservoirs in North America accounts for 20%~85%, and the Sichuan Basin accounts for 27.1%~47.8% (Curtis, 2002; Borjigin et al., 2017). An effective method to determine the adsorbed gas content of shale is methane adsorption experiments (Rexer et al., 2013; Yuan et al., 2014; Ji et al., 2015; Wang et al., 2016a). Currently, the adsorption amount measured by the isothermal adsorption experiment in the laboratory is the excess adsorption amount, which follows Gibbs's excess adsorption behavior (Sakurovs et al., 2007; Bi et al., 2017; Zhou et al., 2018; Dang et al., 2020). However, most of the methane adsorption experiments carried out by scholars far below the in-situ reservoir temperature (80–120 °C) and pressure (> 30 MPa) of China, which cannot accurately reveal the characteristics of shale reservoir methane adsorption (Chareonsuppanimit et al., 2012; Rexer et al., 2013; Yang et al., 2017b; Chen et al., 2018; Dang et al., 2020). For subcritical gas adsorption characterization, the adsorption isotherms have been described using Langmuir, Brunauer-Emmett-Teller (BET), Dubinin-Astakhov (DA), Dubinin-Radushkevich (DR), density functional theory (DFT), and Ono-Kondo models. However, there are obvious differences between supercritical gas and subcritical gas adsorption, and supercritical gas adsorption cannot be directly characterized by these subcritical gas adsorption models (Langmuir, 1918; Brunauer et al., 1938; Astakhov and Dubinin, 1971; Sakurovs et al., 2007; Charoensuppanimit et al., 2016; Bi et al., 2017). It is reported that a modified DR model was found to be superior to the Langmuir model for characterization of supercritical methane adsorption (Rexer et al., 2013). For supercritical carbon dioxide and methane gas adsorption, the DA model is significantly more reliable than the D-R and Ono-Kondo models (Zhou et al., 2019). At high pressure, the difference between the absolute and excess adsorption is not negligible, and an accurate density of adsorbed methane (ρ_{ads}) is crucial to correct the excess adsorption to absolute adsorption (Zhou et al., 2018; Feng et al., 2020; Chen et al., 2021a). However, due to the nature of supercritical gases, it is generally impossible to measure the adsorbed phase density (ρ_{ads}) experimentally (Zhou et al., 2018). Previous literature reported that the ρ_{ads} is considered to be constant at 0.373 g/cm^3 for adsorbent-adsorbate energy greater than the thermal energy (~20 kJ/mol for methane) (Gensterblum et al., 2013). Some scholars considered the ρ_{ads} to be 0.424 g/cm^3 (the density of methane at the boiling point at atmospheric pressure) (Yang et al., 2015).

Shale mineral composition, organic matter (OM), pore structure, water saturation, temperature and pressure characteristics are the main factors affecting the shale adsorption capacity (Hao et al., 2013). The micropores volume and SSA in shale increase with total organic carbon content (TOC). Meanwhile, the adsorption capacity of shale increases

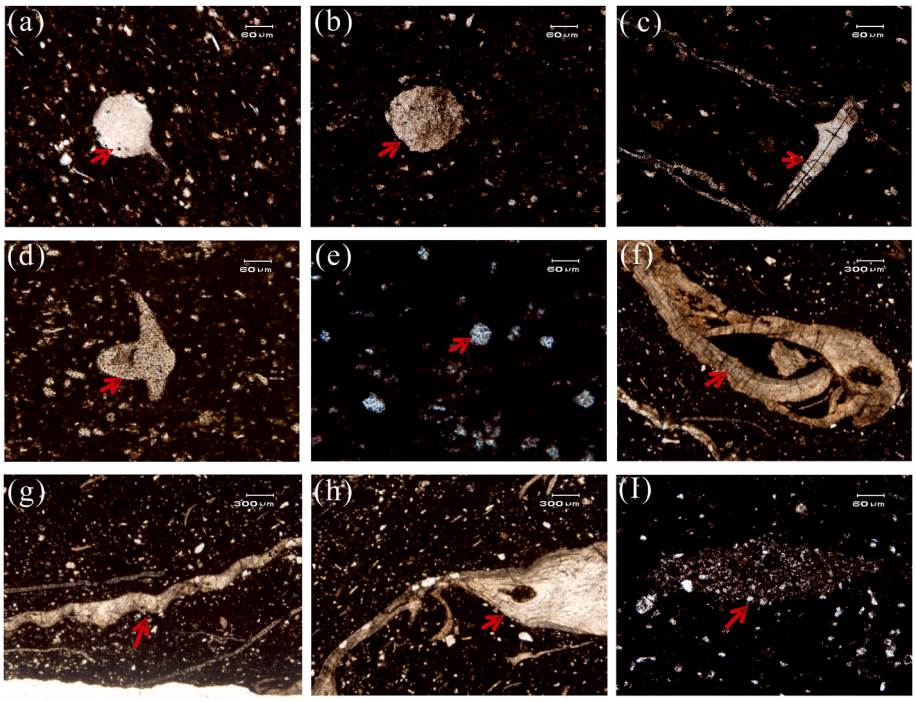

Fig. 2. Typical paleontological fossils in shales of Wufeng-Longmaxi Formation. (a,b) radiolarians; (c,d) spicules; (e) acritarchs; (f) lingula; (g)Hirnantia; (h) brachiopods; and (i) horizontal burrows.

with micropores volume and SSA (Ross and Marc Bustin, 2009; Hao et al., 2013). Most clay minerals with large SSA play a vital role in the adsorption capacity of organic-poor shale under anhydrous conditions (Lu et al., 1995; Heller and Zoback, 2014).

In-situ shale reservoirs usually contain some water, with water saturation varying between 10% and 35% in North American shale gas reservoirs and ranging from 10% to 90% in the Sichuan Basin (Chalmers and Bustin, 2008; Gasparik et al., 2014; Yang et al., 2017a; Zou et al., 2018). The adsorption capacity of Devonian-Mississippian and Jurassic shales in the northeastern British Columbia basin, Canada at equilibrium moisture is 58.3% and 71.5% of that in the dry state, respectively (Hao et al., 2013). Water can exert an important effect on in-situ shale oil/gas reserves and water adsorption characteristics of shale have been systematically and comprehensively studied (Wang and Yu, 2016; Yang et al., 2017a, 2020; Feng et al., 2018). When the relative humidity (RH) value is relatively low, water molecules are directly adsorbed in the hydrophilic clay-associated pore spaces of the shale surface as a monolayer by the van der Waals force. And in the high RH region, the abundance of pores for gas adsorption is progressively blocked by clusters of water and capillary condensation of water molecules (Yang et al., 2020). The amount of adsorbed gas would be overestimated if the water content of the reservoirs is overlooked. However, the previous methane-shale adsorption experiments usually tested at the full moisture-equilibrated shale. Thus, the methane adsorption test on water-bearing shale at the in-situ water saturation is required to obtain a more precise estimate of the adsorbed gas content (Yang et al., 2020).

The characteristics of reservoirs and gas content of shale lithofacies vary substantially, and the shale gas occurrence and content in different lithofacies need to be further investigated. Then, FE-SEM and LPGA experiments were used to fully characterize and clarify the differences in the pore structure of various lithofacies. The shale adsorption capacity was investigated by high temperature and pressure methane adsorption experiments and characterized by supercritical excess adsorption S-L, S-BET, S-DA, S-DR, and Ono-Kondo models. The maximum methane adsorption capacity, the ρ_{ads}, and other parameters were obtained by the S-DA model fitting. In addition, the correlation between shale adsorption capacity and TOC content, mineral composition, and water content were also discussed. Finally, the pattern of shale gas occurrence and content in different lithofacies are summarised based on the mineral composition, OM, pore structure, and water saturation characteristics of various lithofacies.

2. Geological setting

Sichuan Basin is known for its vast natural gas resources, with over 4.0×10^{13} m^3 of shale gas resources, of which about 5.0×10^{12} m^3 of economically recoverable reserves. The Sichuan Basin has undergone multi-stage tectonic movements, with the Himalayan orogeny causing the sedimentary caprocks from the Sinian to the Early Tertiary to be fully folded, forming the present-day tectonic landscape (Wei et al., 2014). It is a diamond-shaped basin with a total area of approximately 1.8×10^5 km^2 (Li et al., 2021; Qian et al., 2022). The Sichuan basin is divided into four hydrocarbon accumulation areas based on the nature of the basement, sedimentary characteristics and hydrocarbon genesis (Li et al., 2022), Fig. 1(a). During the late deposition of the Wufeng Formation, the formation of polar glaciers led to a drop in sea level, and large-scale sea regression occurred in the Yangtze area, and the deep-water retention environment was transformed into shallow-water shelf deposition. In the early stage of the Silurian Longmaxi Formation, a large-scale transgression occurred in the Yangtze region, and the southern Sichuan region was transformed into a deep-water shelf depositional environment; in the middle and late Longmaxi Formation, the sea level in the southern Sichuan region dropped significantly and gradually transformed into a shallow-water continental shelf depositional environment (Zhao et al., 2017; Xiao et al., 2021; Qiu et al., 2022). In addition, radiolarians and spicules are abundant in the early Wufeng-Longmaxi Formation, as illustrated in Fig. 2(a)-(d), indicating a deep-water sedimentary environment. Fossils of planktonic (e.g., Acritarchs) and benthic calcareous organisms (e.g., *brachiopods*, *Lingula*, and *Hirnantia*) have also been found in the Wufeng-Longmaxi Formation, Fig. 2(e)–(h). As shown in Fig. 2(i), trace fossils of horizontal burrows have been found in some wells, which reflects that the depth of sedimentary water bodies in southern Sichuan varies greatly, with both relatively shallow water environments and rather deep water

Table 1
TOC, porosity, bulk density, mineralogical compositions and lithofacies of the Wufeng-Longmaxi Formation, southern Sichuan.

Sample ID	Depth (m)	TOC (%)	Porosity (%)	Bulk density (g/cm^3)	Mineral content (%)						Lithofacies
					Quartz	Feldspar	Calcite	Dolomite	Pyrite	Total Clay	
W8-8	2747.60	3.76	5.61	2.71	66.2	1.9	10.3	8.8	1.5	11.3	SS
L2-3	4309.87	4.14	6.01	2.68	55.8	5.1	4.9	6.5	5.9	21.8	
L6-4	4039.00	4.11	5.81	2.69	59.8	3.3	6.8	12.6	3.0	14.5	
L6-5	4041.45	3.62	4.09	2.68	47.2	6.6	18.7	10.2	2.3	15.0	
W8-5	2743.45	2.55	5.24	2.68	43.9	7.7	4.7	5.0	3.1	35.6	A-SS
W8-6	2737.52	3.54	5.53	2.65	52.1	5.5	2.9	4.4	4.5	30.6	
L2-2	4303.75	2.53	2.26	2.67	44.7	9.8	4.6	9.5	1.5	29.9	
L5-1	4012.98	2.48	3.76	2.68	44.7	8.4	9.0	6.7	3.2	29.0	
L6-3	4029.08	3.56	5.38	2.68	49.3	4.6	3.8	5.0	3.2	34.1	
W8-2	2720.10	2.53	3.24	2.68	25.3	4.2	22	17.7	3.6	27.2	MS
W8-4	2744.95	4.70	5.72	2.64	31.8	3.0	15.6	19.6	8.4	21.6	
W8-7	2734.98	4.20	5.63	2.66	35.4	5.4	10.8	13.5	4.7	30.2	
L5-2	3993.03	3.50	4.66	2.68	34.6	5.6	11.9	10.3	3.1	34.5	
L6-7	4035.05	3.87	3.94	2.67	37.1	4.3	14.3	10.1	4.1	30.1	
W8-1	2716.90	0.46	2.78	2.61	21.9	3.2	9.1	6.9	7.5	51.4	AS
W8-9	2751.31	2.06	3.06	2.64	40.6	4.8	0.9	1.2	1.4	51.1	
L5-3	4005.25	2.38	4.21	2.63	27.0	4.8	5.2	4.0	4.4	54.6	
L5-4	4284.00	2.43	4.50	2.66	36.6	5.0	2.4	6.1	1.0	48.9	

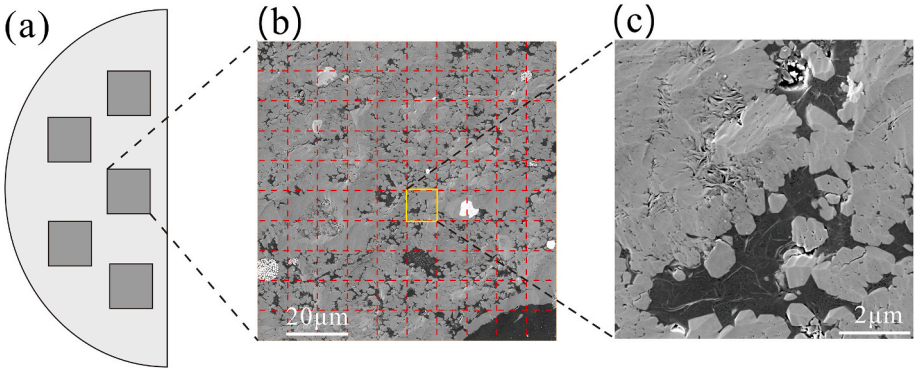

Fig. 3. The operation procedures of SEM image stitching technology.

environments (Nie et al., 2017). Before the Permian, marine sediments dominated the Sichuan Basin, as well as mud shale and carbonate. The Wufeng-Longmaxi Formation generally deposited a set of deep-water organic-rich carbonaceous graptolite shale, with a thickness surpassing 200 m (Gou et al., 2020; Xu et al., 2020a), Fig. 1(b).

3. Samples and methods

3.1. Samples

Samples were collected from four wells in the Luzhou-Weiyuan play, W8, L2, L5 and L6, in the Wufeng-Longmaxi Formation shale, Fig. 1. And the pattern of shale gas enrichment and preservation conditions is basically the same in southern Sichuan (Ma and Xie, 2018). The samples information including depth, porosity, and TOC is listed in Table 1. The porosity was measured by the fluid saturation method. The TOC contents were tested by a CS-600 carbon/sulfur analyzer. The shale samples mineralogical compositions were tested by the X-ray diffractometer RINT-TTR3.

3.2. FE-SEM

The FE-SEM allows the morphology and size of nanoscale pores to be observed directly (Loucks et al., 2012; Chalmers et al., 2012; Yang et al., 2016; Gou et al., 2019). The shale sample was observed using the Crosbeam540 apparatus. Prior to the observation, the surface of the shale sample needs to be finely ground and argon ion polished, and sprayed with gold to enhance the conductivity and obtain a better resolution effect (Xu et al., 2020a; Chandra and Vishal, 2021). The operation process and advantages of SEM image stitching technique can be referred to the study of Li et al. (2021). As illustrated in Fig. 3, five regions (100 μm × 100 μm) were randomly selected on the surface of each sample, each consisting of a 10 × 10 matrix image with a resolution of 4 nm.

3.3. Low-pressure gas adsorption

Shale pore structure parameters (PV, SSA, PSD, porosity, etc.) can be more accurately characterized by CO_2 and N_2 gas adsorption (Wei et al., 2016; Liu et al., 2018; Tripathy et al., 2019; Vishal et al., 2019). The low-pressure N_2 adsorption (LPNA) experiment can well characterize the shale meso-macropores (2–100 nm), and the low-pressure CO_2 adsorption experiment can elaborated explain the shale micropores (0–2 nm) characteristics. In this study, LPGA experiments were carried out by using a BeiShiDe PS2 fully automated specific surface area analyzer. Prior to the LPGA experiment, the core samples were crushed to 60–80 mesh (180–250 μm), and dried at 110 °C for 24 h, weighed about 5 g, and put into the analyzer workstation for vacuum degassing. N_2 adsorption experiments were conducted at 77 K, and CO_2 were conducted at 273 K, respectively. The pore structure parameters (PV, SSA, PSD, etc.) of shale micropores are accurately characterized by CO_2 adsorption experiments and density functional theory (DFT). Meanwhile, those of meso-macropores were obtained by N_2 adsorption experiments combined with BJH and multi-point BET models (Wei et al., 2016; Chen et al., 2017; Pang et al., 2021).

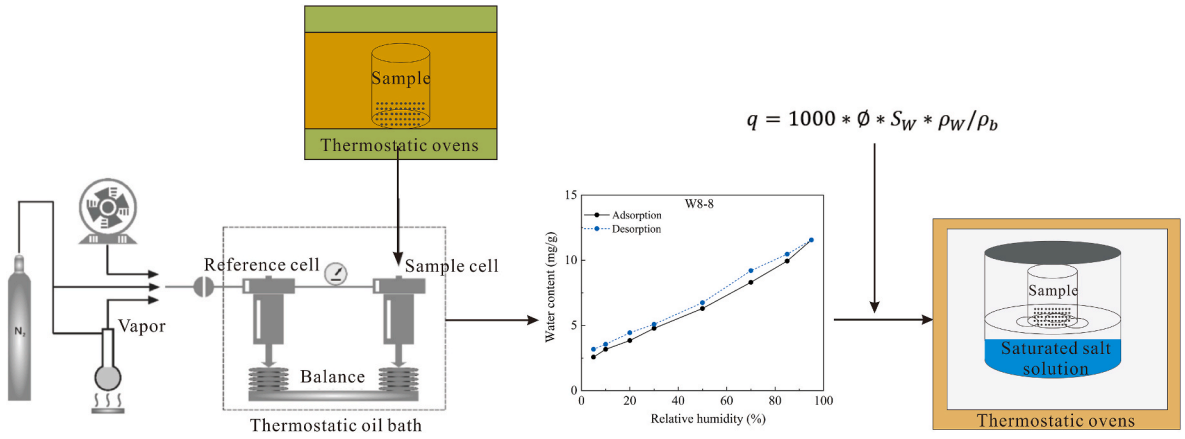

Fig. 4. Diagram of the process of water content restoring experiments on shale samples.

3.4. Water content restoring

Shale cores taken out of the ground are exposed to air for long periods of time, and their original moisture suffers from fugitive loss. To maintain the water content of the actual in-situ shale reservoir, it is necessary to restore the water content of the sample according to the water saturation data obtained at the coring site. The main experimental methods are as follows:

(1) Approximately 1 g of dry shale sample in 60–80 mesh was put into the workstation and degassed. Then, shale moisture adsorption was carried out at 50 °C using the dynamic weight method to obtain the amount of moisture adsorbed at different relative humidities. The experimental apparatus is BeiShiDe Vacuum Vapor/Gas Sorption Analyzer. An elaborated explanation of the workflow and function of the experimental apparatus can be found in Dang et al. (2021). In this work, 8 relative humidity steps were measured to establish isotherms, and the equilibrium condition was set to 0.01%/60 min. When all samples' adsorption/desorption equilibrium was reached, the next relative humidity step was automatically entered.

(2) The original water content of the sample is determined by the water saturation and porosity of the sample measured at the coring site, and it is matched with the water adsorption amount to obtain the relative humidity required to restore the water saturation under the in-situ conditions. Then, the corresponding saturated salt solution was used to restore the water content of the dried sample in a closed constant temperature (50 °C) environment, the experiment procedure is demonstrated in Fig. 4. The water saturation, original water content, relative humidity and saturated salt solution type of shale samples are listed in Table 3. The reason for restoring sample water content via saturated salt solutions is that the binding of water to the shale samples is stable compared to the dynamic weight method, which facilitates the subsequent LPNA experiments and high-pressure methane adsorption experiments on wet shale samples. The original water content can be determined by Eq. (1):

$$q = 1000 * \varphi * S_W * \rho_W/\rho_b \quad (1)$$

where q is water content, mg/g; φ is porosity, %, listed in Table 1; S_W is water saturation, %, listed in Table 3; ρ_W is the water density, regarded as 1 g/cm^3; ρ_b is the bulk density of shale, g/cm^3, listed in Table 1.

3.5. High-pressure methane adsorption

Approximately 130 g of 60–80 mesh dry shale samples were put into the BeiShiDe 3H–2000 PH adsorption equipment to carry out the methane adsorption measurements. An elaborated explanation of the workflow and function of the experimental apparatus can be found in the research of Shen et al. (2021). To match the in-situ reservoir pressure as much as possible, the highest pressure of experimental reached 51 MPa in this study. Two samples, W8-6 and L6-3, were selected for high-pressure (0–51 MPa) methane adsorption experiments at different temperatures (313.15 K, 333.15 K and 353.65 K) to investigate the effect of temperature. Furthermore, to obtain actual methane adsorption characteristics under in-situ reservoir water-bearing conditions, water content restoring shale samples of W8 well were selected for high-pressure methane adsorption tests at 60 °C without degassing prior to the experiment.

4. Modeling study for gas content

4.1. Supercritical adsorption characterization model

Many scholars have proposed various subcritical gas adsorption isotherm models to characterize shale methane adsorption based on different theoretical assumptions such as monolayer adsorption, multilayer adsorption, and adsorption potential (micropore filling, volume filling) (Langmuir, 1918; Brunauer et al., 1938; Astakhov and Dubinin, 1971; Sakurovs et al., 2007; Charoensuppanimit et al., 2016; Bi et al., 2017). Nevertheless, supercritical shale methane adsorption is characterized by a decrease in excess adsorption amount during the high-pressure phase, the above absolute adsorption isotherm models are no longer applicable, and a correction term needs to be added according to Gibbs' excess adsorption theory (Gibbs, 1878; Dang et al., 2020; Shen et al., 2021). In this research, the commonly used Langmuir model, Brunauer-Emmett-Teller (BET) model, Dubinin-Astakhov (DA) model, Dubinin-Radushkevich (DR) model and Ono-Kondo model were selected, and the excess adsorption correction term was added to evaluate the optimal supercritical methane adsorption isotherm model based on experimental data.

4.1.1. A modified Langmuir-based supercritical methane excess adsorption model (S-L model)

The Langmuir model assumes that methane molecules are adsorbed in a single layer on the adsorbent surface, that the surface of adsorbent is energetically homogeneous, and that one mass is adsorbed at each adsorption site (Langmuir, 1918). The Langmuir model is generally depicted as follows:

$$n_{abs} = \frac{V_L P}{P + P_L} \quad (2)$$

where n_{abs} is absolute adsorption amount, m^3/t; V_L is the Langmuir volume, m^3/t; P is the adsorption equilibrium pressure, MPa; P_L is the

Langmuir pressure, the corresponding pressure when the adsorption amount reaches half of V_L, Mpa.

The Langmuir model's adsorption isotherm exhibits I-type isotherm adsorption behavior; which is in conflict with the fact that the amount of methane gas adsorbed decreases under supercritical conditions. The supercritical shale methane adsorption follows the Gibbs's excess adsorption behavior, so the excess adsorption correction term is introduced, and the excess adsorption isotherm model is obtained as follows:

$$n_{ex} = \frac{V_L P}{P + P_L}\left(1 - \frac{\rho_{gas}}{\rho_{ads}}\right) \tag{3}$$

where n_{ex} is the excess adsorption amount, m^3/t; ρ_{ads} is methane density of adsorbed phase, g/cm^3; ρ_{gas} is methane density of free phase, g/cm^3.

4.1.2. A modified BET-based supercritical methane excess adsorption model (S-BET model)

The well-known BET model assumes that gas molecules are adsorbed on solid surfaces in multiple layers (Brunauer et al., 1938), with the equation:

$$n_{abs} = \frac{V_{BET} C P}{(P_0 - P)[1 + (C-1)(P/P_0)]} \tag{4}$$

where V_{BET} is the maximum monolayer adsorption volume of BET model, m^3/t; C is a constant, dimensionless; P_0 is the saturation vapor pressure, MPa.

Similarly, the introduction of an excess adsorption correction term gives the following supercritical BET excess adsorption model:

$$n_{ex} = \frac{V_{BET} C P}{(P_0 - P)[1 + (C-1)(P/P_0)]}\cdot\left(1 - \frac{\rho_{gas}}{\rho_{ads}}\right) \tag{5}$$

Eq. (5) can be simplified and rearranged as (Dang et al., 2020):

$$n_{ex} = \frac{P}{k_1 + k_2 P + k_3 P^2}\cdot\left(1 - \frac{\rho_{gas}}{\rho_{ads}}\right) \tag{6}$$

where k_1, k_2, and k_3 are the three fitted parameters, and defined as: $k_1 = P_0/V_{BET}C$; $k_2 = (C-2)/V_{BET}C$; $k_3 = (1-C)/V_{BET}CP_0$. However, the saturation vapor pressure cannot be accurately determined under supercritical phase, and when the gas density is used in place of the gas pressure, then Eq. (6) becomes

$$n_{ex} = \frac{\rho_{gas}}{k_1 + k_2 \rho_{gas} + k_3 \rho_{gas}^2}\cdot\left(1 - \frac{\rho_{gas}}{\rho_{ads}}\right) \tag{7}$$

4.1.3. Modified supercritical methane excess adsorption models based on the DA and DR model (S-DA, S-DR)

Strongly heterogeneous shale has a complicated pore structure and a wide distribution of pore sizes ranging from a few to several hundred nanometres (Loucks et al., 2009; Teng et al., 2022). The Polanyi theory assumes that the methane molecules is sequentially filled into the micropores according to the size of the pore adsorption potential. This model, which takes into consideration the surface heterogeneity, can more accurately describe the gas adsorption behavior of heterogeneous shale (Astakhov and Dubinin, 1971; Dang et al., 2020). The Dubinin-Astakhov (DA) micropore filling model derived based on the Polanyi theory is as follows:

$$n_{abs} = V_M \exp\left\{-D\left[\ln\left(\frac{P_0}{P}\right)\right]^n\right\} \tag{8}$$

where V_M is the maximum adsorption volume of micropore filling of DA model, m^3/t; D is pore structure parameter; n is a constant.

As noted above, the saturation vapor pressure cannot be accurately determined under the supercritical phase and the gas pressure P_0 and P are replaced with the methane density of adsorbed phase ρ_{ads} and free phase ρ_{gas}, respectively. Meanwhile, taking the Gibbs excess adsorption behavior into account and establish the supercritical Dubinin-Astakhov (S-DA) excess adsorption model as follows:

$$n_{ex} = V_M \exp\left\{-D\left[\ln\left(\frac{\rho_{ads}}{\rho_{gas}}\right)\right]^n\right\}\cdot\left(1 - \frac{\rho_{gas}}{\rho_{ads}}\right) \tag{9}$$

When n = 2, Eq. (9) becomes the supercritical Dubinin-Radushkevich (S-DR) excess model, which is derived from Dubinin's volume filling theory (Sakurovs et al., 2007; Song et al., 2018). The expressions are as follows:

$$n_{ex} = V_M \exp\left\{-D\left[\ln\left(\frac{\rho_{ads}}{\rho_{gas}}\right)\right]^2\right\}\cdot\left(1 - \frac{\rho_{gas}}{\rho_{ads}}\right) \tag{10}$$

4.1.4. Ono-Kondo supercritical methane adsorption model based on multilayer adsorption theory

The Ono-Kondo model assumes a three-dimensional lattice of adsorbate molecules in contact with a planar adsorbent surface (Xiong et al., 2020). Shale pores can be characterized simply as silt pores (Bi et al., 2017). The expressions are as follows:

$$n_{abs} = V_0 \frac{2\rho_{gas}\left[1 - \exp\left(\frac{\varepsilon_s}{k\cdot T}\right)\right]}{\frac{\rho_{ads}\rho_{gas}}{\rho_{ads} - \rho_{gas}} + \rho_{ads}\exp\left(\frac{\varepsilon_s}{k\cdot T}\right)} \tag{11}$$

Where V_0 is the saturated adsorption capacity of the monolayer, m^3/t; k is the Boltzmann's constant, 1.38×10^{-23} J/K; ε_s is the energy of the methane−pore interaction; T is the temperature of methane adsorption experiment, K.

Similarly, the introduction of an excess adsorption correction term gives the following supercritical excess Ono-Kondo model:

$$n_{ex} = V_0 \frac{2\rho_{gas}\left[1 - \exp\left(\frac{\varepsilon_s}{k\cdot T}\right)\right]}{\frac{\rho_{ads}\rho_{gas}}{\rho_{ads} - \rho_{gas}} + \rho_{ads}\exp\left(\frac{\varepsilon_s}{k\cdot T}\right)}\cdot\left(1 - \frac{\rho_{gas}}{\rho_{ads}}\right) \tag{12}$$

4.2. Density of adsorption methane

An accurate density of adsorbed methane (ρ_{ads}) is crucial to correct the excess adsorption to absolute adsorption (Zhou et al., 2018; Chen et al., 2021b), however, it is generally impossible to measure the ρ_{ads} experimentally. The ρ_{ads} is assumed as either 0.373 g/cm^3 (the van der Waals density) or 0.424 g/cm^3 in previous reports (Sakurovs et al., 2007; Bi et al., 2017; Han et al., 2021), but the ρ_{ads} varies significantly among samples and will lead to discrepancies with the actual data. Besides, the excess adsorption amount is linearly related to the methane density of the free phase ρ_{gas}, and the ρ_{ads} is the value of the intersection of the straight line with the methane density of the free phase axis (Zhou et al., 2018). For all samples, this method may not be the most accurate way to estimate the ρ_{ads}, and the results are often higher than the real data (Zhou et al., 2018). Furthermore, regarding the ρ_{ads} as an undetermined parameter, the value obtained by mathematically optimizing a supercritical methane excess adsorption model combined with experimental data is consistent with the thermodynamic properties of methane and minimizes the discrepancies from the experimental data (Feng et al., 2020; Zhou et al., 2018).

4.3. Prediction model for adsorbed gas

Currently, experimental measurements are all excess methane adsorption amount which is the portion where the gas density in the adsorbed phase exceeds the density of the free phase according to Gibbs' theory (Gibbs, 1878; Feng et al., 2020). Excess adsorption is a function of absolute adsorption:

$$n_{abs} = n_{ex} \Big/ \left(1 - \frac{\rho_{gas}}{\rho_{ads}}\right) \tag{13}$$

The S-DA excess adsorption model works best and will be elaborated

in Section 5.4. Meanwhile, excess adsorption and absolute adsorption differ significantly under in-situ shale reservoir conditions. The absolut adsorption amount model are established by combining Eq. (9) and Eq. (13) as follows:

$$n_{abs} = V_M \exp\left\{ -D\left[\ln\left(\frac{\rho_{ads}}{\rho_{gas}}\right)\right]^n \right\} \tag{14}$$

Both the maximum adsorption volume of micropore filling V_M and the methane density of adsorbed phase ρ_{ads} are dependent on temperature (Yang et al., 2017b; Chen et al., 2018; Han et al., 2021). Due to methane adsorption saturation at high pressure, the ρ_{ads} increases and tends to stabilize (Tang et al., 2019; Feng et al., 2020), thus, it is assumed that the ρ_{ads} is only a function of temperature $\rho_{ads}(T)$. The methane density of free phase ρ_{gas} is dependent on both temperature and pressure, however the gas state of methane under in-situ reservoir deviates from the ideal gas state and cannot be obtained directly using the PVT equation of ideal gas. In this study, the ρ_{gas} at a given temperature and equilibrium pressure is available at the NIST (https://webbook.nist.gov/chemistry/fluid/) (Dang et al., 2020), and the applicable temperature and pressure ranges are 90.6941–625.0 K and 0–1000 MPa respectively. The relationship between the prediction model of adsorbed gas and reservoir temperature and pressure is obtained by substituting parameters such as $V_M(T)$, $\rho_{ads}(T)$, and $\rho_{gas}(P,T)$ into Eq. (14):

$$n_{abs} = V_M(T) exp\left\{ -D\left[ln\left(\frac{\rho_{ads}(T)}{\rho_{gas}(P,T)}\right)\right]^n \right\} \tag{15}$$

4.4. Prediction model for free gas

In previous studies, the prediction model for free gas is usually established without taking the pore space occupied by adsorbed gas into account (Ambrose et al., 2012), and over-mature shale gas reservoirs contain almost no liquid hydrocarbons (Li et al., 2015), the equation for free gas is expressed as follows:

$$G_f^{con} = \frac{\varphi\cdot(1-S_w)}{\rho_b\cdot B_g} \tag{16}$$

where G_f^{con} is the free gas content at standard temperature and pressure (STP) without taking the pore space occupied by adsorbed gas into account, m^3/t; and B_g is the coefficient of gas volume, dimensionless, and it can be calculated as follows:

$$B_g = \frac{\rho_{STP}}{\rho_{gas}} \tag{17}$$

where ρ_{STP} is methane density at STP.

Then, substitute Eq. (17) into Eq. (16), then it becomes

$$G_f^{con} = \frac{\varphi\cdot\rho_{gas}\cdot(1-S_w)}{\rho_b\cdot\rho_{STP}} \tag{18}$$

The adsorbed gas volume is quite small and negligible at lower pressures; whereas at high pressure, it is impossible to ignore the volume of the adsorbed gas. Thus, the amount of pore space filled by the adsorbed gas need be subtracted to obtain the actual free gas content:

$$G_f = G_f^{con} - \frac{\rho_{gas}\cdot V_a}{\rho_{STP}} \tag{19}$$

where V_a is volume of the adsorbed gas, cm^3/g; and it can be calculated by Eq. (20)

$$V_a = \frac{n_{abs}\cdot\rho_{STP}}{\rho_{ads}} \tag{20}$$

Combining Eq. (15), Eq. (18), Eq. (19) and Eq. (20), the equation for the actual free gas is rearranged as:

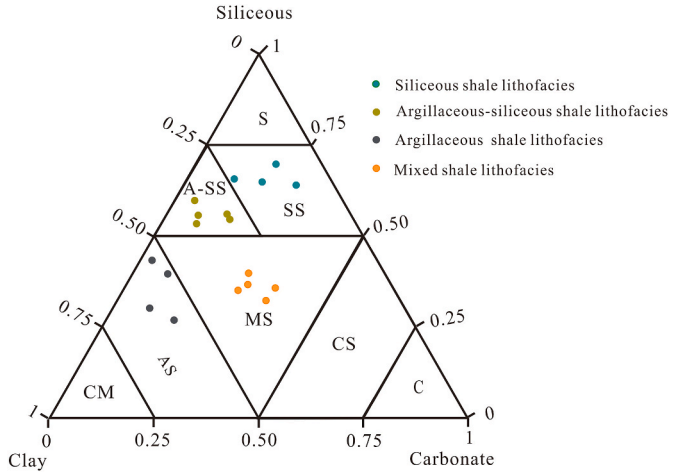

Fig. 5. A three-end diagram of lithofacies classification.

$$G_f = \frac{\varphi\cdot\rho_{gas}\cdot(1-S_w)}{\rho_b\cdot\rho_{STP}} - V_M \exp\left\{ -D\left[\ln\left(\frac{\rho_{ads}}{\rho_{gas}}\right)\right]^n \right\}\cdot\frac{\rho_{gas}}{\rho_{ads}} \tag{21}$$

The relationship between the prediction model of free gas and reservoir temperature and pressure is obtained by substituting parameters such as $V_M(T)$, $\rho_{ads}(T)$, and $\rho_{gas}(P,T)$ into Eq. (21)

$$G_f = \frac{\varphi\cdot\rho_{gas}(P,T)\cdot(1-S_w)}{\rho_b\cdot\rho_{STP}} - V_M(T) exp\left\{ -D\left[ln\left(\frac{\rho_{ads}(T)}{\rho_{gas}(P,T)}\right)\right]^n \right\}\cdot\frac{\rho_{gas}(P,T)}{\rho_{ads}(T)} \tag{22}$$

5. Results and discussion

5.1. Geochemical and lithofacies characteristics

Quartz and clay minerals predominate in the Wufeng-Longmaxi Formation shale in southern Sichuan, listed in Table 1. Typical classification schemes are based on siliceous minerals (quartz and feldspar), carbonate minerals, and clay minerals (Zhang et al., 2020). As illustrated in Fig. 5, the Wufeng-Longmaxi Shales mainly consiste four lithofacies: siliceous shale lithofacies (SS), argillaceous-siliceous shale lithofacies (A-SS), mixed shale lithofacies (MS), and argillaceous shale lithofacies (AS). Both the SS shale and A-SS are quartz-rich, with contents ranging from 47.2% to 66.2% and 44.7%–52.1%, with an average of 57.3% and 46.9%, respectively. It is noteworthy that the clay mineral content in A-SS is relative high, ranging from 29.0% to 35.6% with an average of 31.8%. The MS consist of moderate quartz content and clay mineral content, with an average of 32.8% and 28.7%, respectively. The AS is dominated by clay, which varies between 48.9% and 54.6%.

The TOC content is highest in siliceous shale, ranging from 3.62% to 4.14%, averaging 3.91%; followed by mixed shale and argillaceous-siliceous shale, averaging 3.76% and 2.93%, respectively. The argillaceous shale possess the lowest TOC, varing between 0.46% and 2.43%, averaging 1.83%. Moreover, the clay content of siliceous shale, mixed shale, argillaceous-siliceous shale, and argillaceous shale increase sequentially, with an average of 15.65%, 28.72%, 31.84% and 51.5%, respectively.

5.2. Shale lithofacies and pore characteristics

5.2.1. OM pores

Pyrobitumen and penstones make up more than 90% of the OM in the Wufeng-Longmaxi Shale, which also contains graptolites, vitrinite-like particles, and acritarchs (Teng et al., 2022). Pyrobitumen filled pore sapce between brittle mineral and mixed with ductile clay

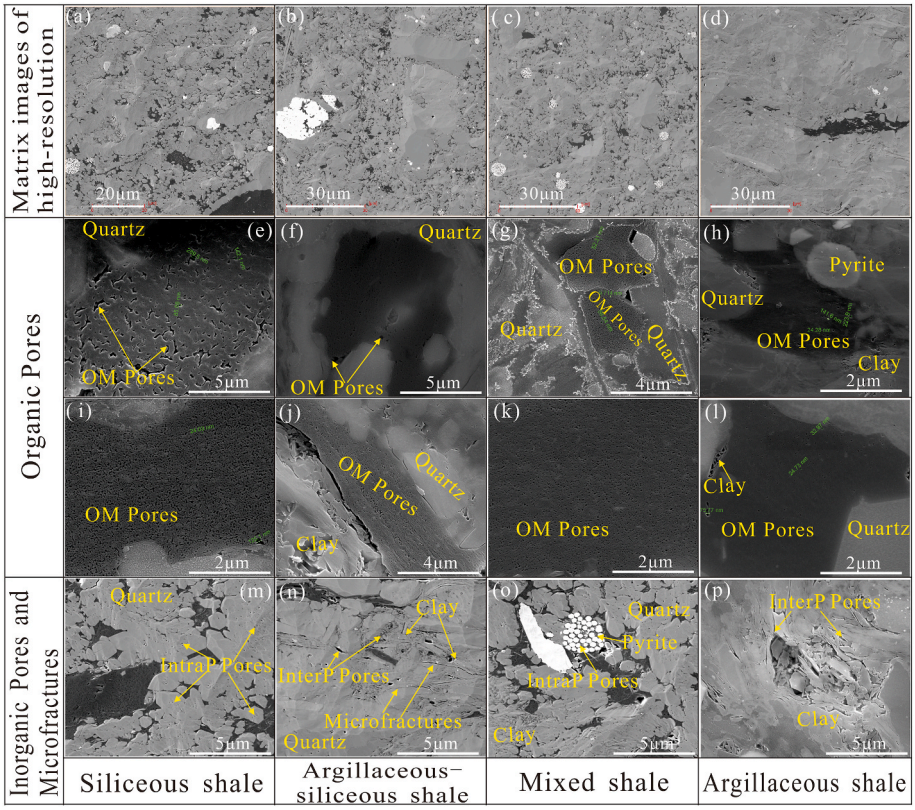

Fig. 6. FE-SEM images for shale samples of Wufeng-Longmaxi Formation, southern Sichuan.

minerals, Fig. 6(a)-(d) and Fig. 6(m)–(o). The OM pores are continuously distributed in the interior or edge of the OM in a large area, and the pore shapes are oval, bubble-like, or sponge-like with sizes ranging from a few to several hundred nanometres, with good connectivity, Fig. 6(e)–(l). The amount of OM pores in siliceous and mixed shale is more than that of argillaceous-siliceous and argillaceous shale due to the abundance of OM, as illustrated in Fig. 6(a)–(d). The OM pores have larger SSA because of irregular boundaries, which can provide more adsorption sites (Chalmers and Bustin, 2008; Li et al., 2015; Chen et al., 2021). Thus, abundant OM pores facilitate enhancing the shale adsorption capacity.

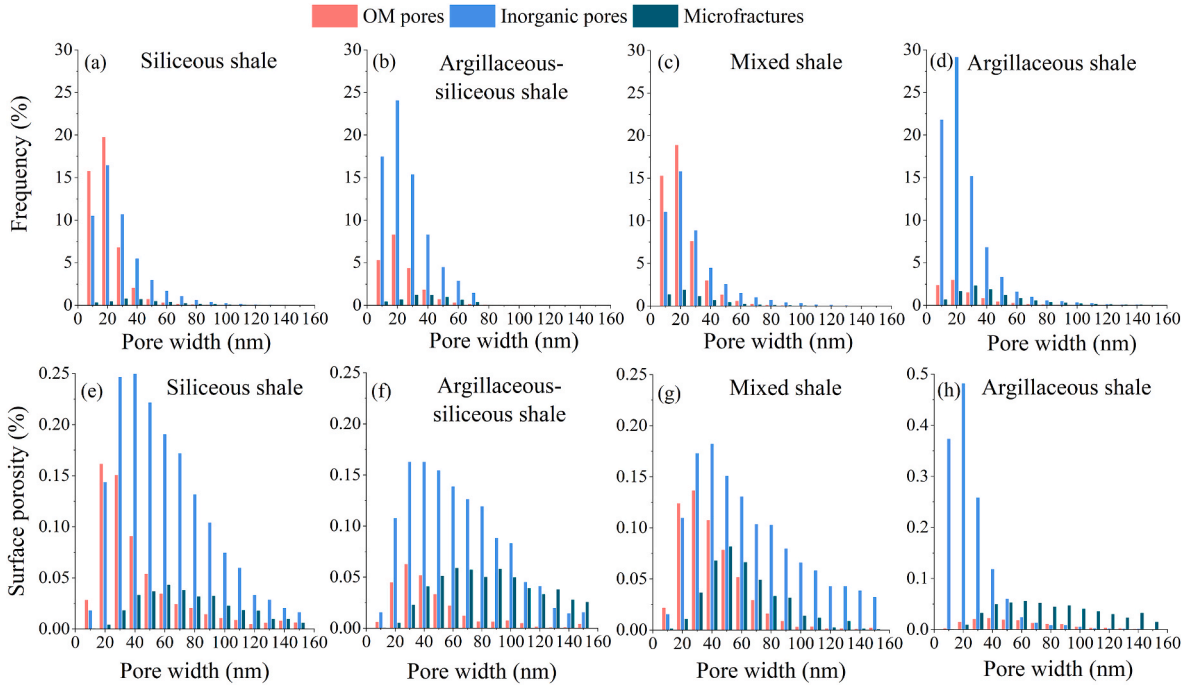

Fig. 7. PSD and surface porosity characteristics of different shale lithofacies calculated from SEM images.

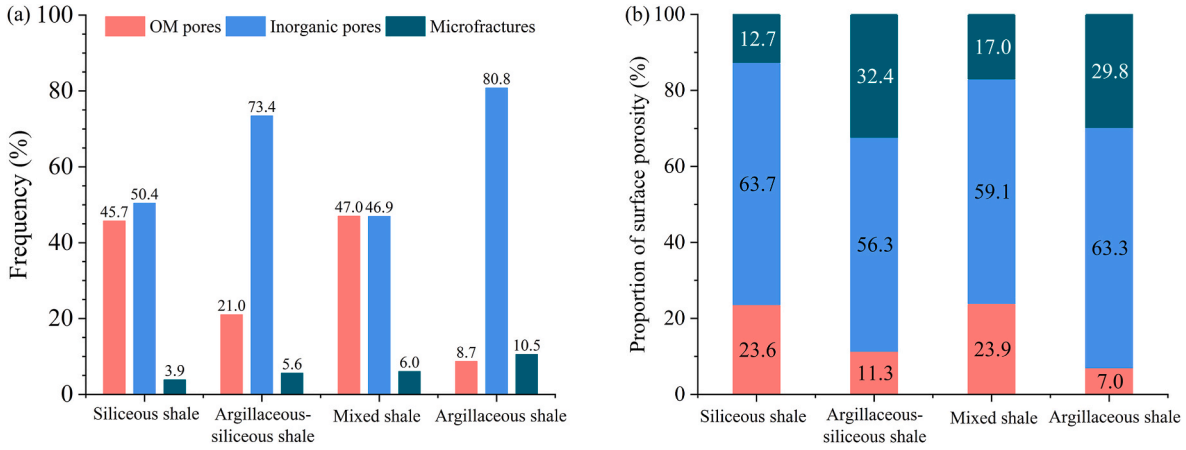

Fig. 8. Pore frequency and proportion of surface porosity characteristics of different shale lithofacies calculated from SEM images. (a) Pore frequency; (b) Proportion of surface porosity.

5.2.2. *Interparticle (InterP) pores*

The edges of brittle minerals, such as quartz, calcite, and dolomite in siliceous and mixed shale, are frequently where the interP pores are found, and the pore shapes are triangular or polygonal, Fig. 6(m) and (o). Moreover, interP pores associated with clay are usually found in argillaceous-siliceous and argillaceous shale, with triangle or slit shapes, as demonstrated in Fig. 6(n) and (p).

5.2.3. *Intraparticle (IntraP) pores*

On the surface of the particles, there are isolated intraP pores, in the shape of triangular or elliptical, and are mainly formed by the dissolution of quartz and carbonate minerals by acidic fluids, Fig. 6(m)–(p) (Xu et al., 2020a; Li et al., 2021). The intraP pores are generally less than 300 nm. In addition, pyrite framboids are common in the Wufeng-Longmaxi Shale. The non-compact aggregation of pyrite crystals during growth creates the pyrite intraP pores, which are typically fewer than 300 nm in size, as shown in Fig. 6(a), (c), and 6(o).

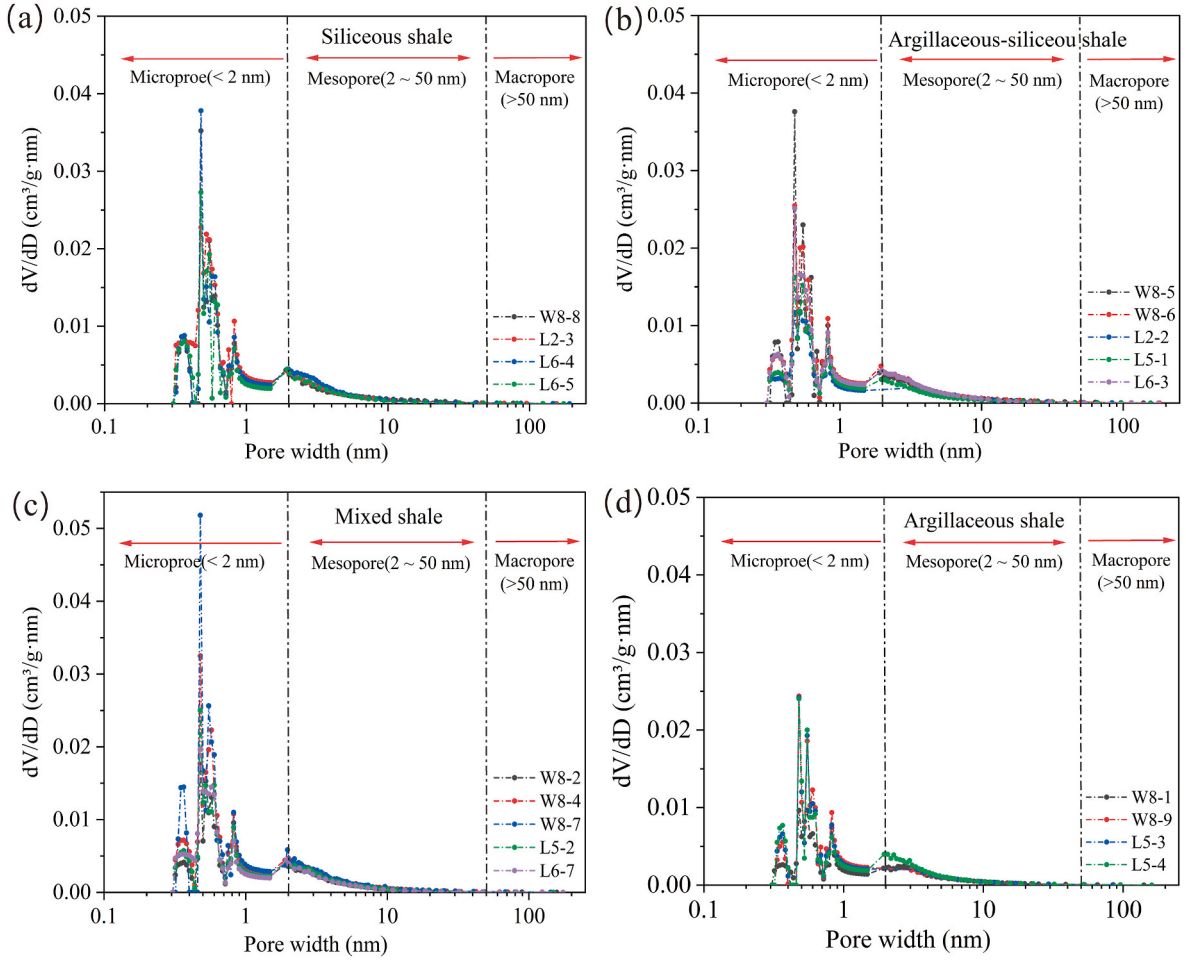

Fig. 9. PSD characteristics of different lithofacies.

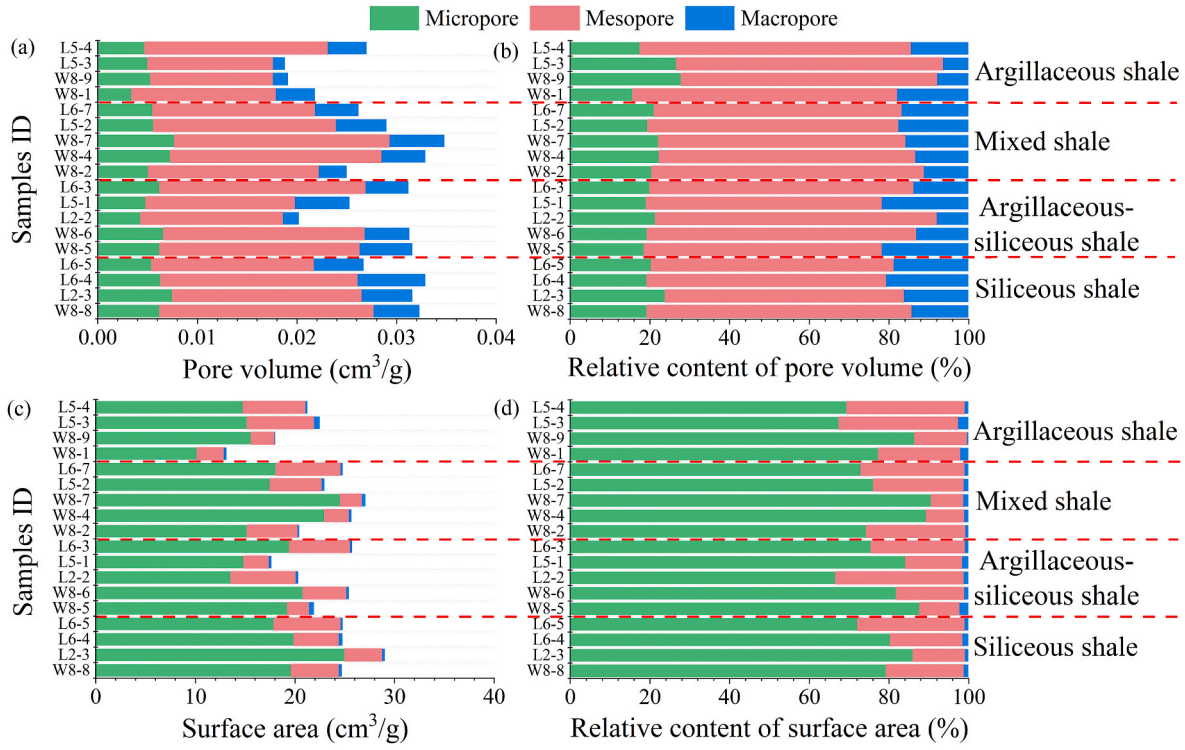

Fig. 10. PV, SSA, and their percentage distribution for different pore sizes of the Wufeng-Longmaxi Shale. (a) PV; (b) Relative content of PV; (c) SSA; (d) Relative content of SSA.

5.2.4. *Microfractures*

Microfractures are conducive to enhancing the shale reservoirs storage capacity, and the microfracture network is useful to improve the seepage capacity and facilitate the accumulation of natural gas because of its good connectivity (Xu et al., 2020b). Microfractures among particles are most developed in the reservoir, which are influenced by the particles and are formed along the interface of mineral particles or OM. These microfractures generally do not extend far and the distance between the connecting microfractures is depended on the size of the particles, with fracture aperture commonly ranging from 0.01 μm to 30 μm.

5.2.5. *Correlation between shale lithofacies and pore characteristics*

Various pores and microfractures in shale samples from Wufeng-Longmaxi were identified and quantitatively characterized by SEM images (Li et al., 2021). However, it should be noted that only organic pores, inorganic pores and microcracks with pore width larger than 10 nm were identified and counted in the SEM images due to the limitation of resolution. As demonstarted in Fig. 7(a) and (c) and Fig. 8(a), the frequency distribution characteristics of OM pores and inorganic pores of siliceous shale and mixed shale are similar, most OM pores are found in the range of 10–40 nm, accounting for 45.7% and 50.4%, respectively. The majority of inorganic pores are found in the range of 10–50 nm, accounting for 50.4% and 46.9%, respectively; the number of microfractures is less, 3.9% and 6.0%, respectively. However, the number of OM pores is relatively small in argillaceous-siliceous shale and argillaceous shale, accounting for 21% and 8.7% respectively; the number of inorganic pores is large, accounting for more than 70%,

Table 2
Pore Characteristic Parameters of the Wufeng-Longmaxi Shale Samples, southern Sichuan.

Sample ID	Pore volume (cm^3/g)				Surface area (m^2/g)				Lithofacies
	Micropore	Mesopores	Macropores	Total	Micropore	Mesopores	Macropores	Total	
W8-8	0.0062	0.0215	0.0046	0.0324	19.578	4.837	0.288	24.703	SS
L2-3	0.0075	0.0190	0.0051	0.0317	24.972	3.798	0.256	29.026	
L6-4	0.0063	0.0198	0.0068	0.0329	19.887	4.515	0.369	24.771	
L6-5	0.0054	0.0163	0.0050	0.0268	17.875	6.694	0.237	24.806	
W8-5	0.0062	0.0201	0.0053	0.0316	19.217	2.206	0.498	21.921	A-SS
W8-6	0.0066	0.0202	0.0045	0.0313	20.792	4.365	0.262	25.419	
L2-2	0.0043	0.0143	0.0016	0.0202	13.531	6.559	0.239	20.329	
L5-1	0.0048	0.0150	0.0055	0.0253	14.845	2.529	0.273	17.647	
L6-3	0.0062	0.0207	0.0043	0.0312	19.428	6.098	0.221	25.747	
W8-2	0.0051	0.0171	0.0028	0.0250	15.176	5.102	0.150	20.428	MS
W8-4	0.0073	0.0212	0.0044	0.0329	22.930	2.490	0.271	25.691	
W8-7	0.0077	0.0216	0.0055	0.0348	24.540	2.189	0.350	27.079	
L5-2	0.0056	0.0183	0.0051	0.0289	17.455	5.225	0.271	22.951	
L6-7	0.0055	0.0163	0.0044	0.0262	18.078	6.491	0.237	24.806	
W8-1	0.0034	0.0145	0.0039	0.0218	10.143	2.715	0.267	13.125	AS
W8-9	0.0053	0.0123	0.0015	0.0191	15.588	2.379	0.070	18.037	
L5-3	0.0050	0.0126	0.0012	0.0188	15.174	6.754	0.581	22.509	
L5-4	0.0047	0.0184	0.0039	0.0270	14.760	6.311	0.194	21.265	

Table 3
Water saturation, original water content, relative humidity and saturated salt solution type of shale samples.

Sample ID	Water saturation (%)	Original water content (mg/g)	Relative humidity (%)	Saturated salt solution (50 °C)
W8-8	27.78	5.75	50	NaBr
L2-3	31.79	7.13	30	$MgCl_2$
L6-4	32.89	7.10	30	$MgCl_2$
L6-5	29.73	4.54	10	LiCl
W8-5	59.95	11.72	85	KCl
W8-6	45.12	9.42	50	NaBr
L5-1	27.88	3.91	30	$MgCl_2$
L6-3	41.04	8.24	50	NaBr
W8-2	53.62	11.92	85	KCl
W8-4	40.60	10.17	50	NaBr
W8-7	49.98	12.31	50	NaBr
L5-2	32.92	5.72	30	$MgCl_2$
L6-7	28.00	4.13	10	LiCl
W8-1	65.67	11.25	70	NaCl
L5-4	55.00	9.30	30	$MgCl_2$

mainly distributed in the range of 10–60 nm; and microfractures account for 5.6% and 10.5% respectively; as illustrated in Fig. 7(b), (d) and Fig. 8 (a).

The surface porosity distribution characteristics of siliceous and mixed shale are similar, with OM pore face porosity accounting for about 24%, provided by organic pores in the range of 20–80 nm. Inorganic pore face porosity accounts for 63.7% and 59.1%, respectively, and is provided by OM pores ranging from 20 to 150 nm; microfractures account for 12.7% and 17.0%, respectively, as depicted in Fig. 7(e), (g), and 8(b). However, the OM pore surface porosity of argillaceous-siliceous shale and argillaceous shale is only 11.3% and 7.0%; provided by OM pores in the range of 20–70 nm. Inorganic pore face porosity is 56.3% and 63.3%, respectively, and microfractures are 12.7% and 17.0%, respectively, Fig. 7(f), (h) and 8(b). Compared with the other lithofacies, the surface porosity of inorganic pores in argillaceous shale is mainly contributed by the pores ranging from 10 to 40 nm, Fig. 7(e)–(h). The reason is that the pore space in argillaceous shale is easily reduced by compaction due to clay-rich shale lacking a siliceous frame that is more resistant to compression (Guo et al., 2020).

Pore structure parameters of the Wufeng-Longmaxi Shale are obtained based on the CO_2 adsorption and NLDFT model, as well as N_2 adsorption, BJH model, and BET model. As illustrated in Fig. 9, the PSD characteristics of the different shale lithofacies are similar. The PV of the shale samples vary between 0.0188 and 0.0348 cm^3/g, with mesopores contributing more than 60% of the PV; followed by micropores accounting for 20%. The total SSA ranges from 13.125 to 29.026 m^2/g, with micropores providing more than 75% of the SSA, followed by mesopores, as shown in Figs. 9 and 10, and Table 2.

The siliceous shale has the largest PV and SSA, with a total PV varying between 0.0268 and 0.0329 cm^3/g (average 0.0310 cm^3/g) and a total SSA ranging from 24.703 to 29.026 m^2/g (average 25.827 m^2/g). The total PV of the argillaceous-siliceous shale ranges from 0.0202 to 0.0343 cm^3/g, averaging 0.0289 cm^3/g; and the total SSA varies between 17.647 and 25.747 m^2/g, averaging 22.213 m^2/g. The total PV of the mixed shale ranges from 0.0250 to 0.0348 cm^3/g, averaging 0.0296 cm^3/g; and the total SSA varies between 20.428 and 27.079 m^2/g, averaging 24.191 m^2/g. The PV and SSA are lowest in argillaceous shale, with a total PV varying between 0.0188 and 0.0270 cm^3/g, averaging 0.0217 cm^3/g; and a total SSA ranging from 13.125 to 22.509 m^2/g, averaging 18.734 m^2/g.

5.3. Shale lithofacies and water content

Shale water saturation is positively correlate with clay content, with water saturation increasing with clay mineral content, as shown in Fig. 11(a). The reason is that clay minerals possess abundant hydrophilic sites, which facilitate the adsorption of water molecules (Roshan et al., 2015; Shen et al., 2019; Wang et al., 2019). Furthermore, Fig. 11(b) demonstrates the apparent disparity in the water saturation of different shale lithofacies, with siliceous shale possessing the lowest water saturation of 30% due to its lowest clay content, and argillaceous shale having the highest water saturation of 60% due to its highest clay content.

5.4. Characteristics of high-pressure methane adsorption and evaluation of supercritical adsorption models

5.4.1. Characteristics of high-pressure methane adsorption

The Wufeng-Longmaxi Shale samples exhibit similar high-pressure methane adsorption characteristics. However, the shale adsorption amounts varies significantly from sample to sample due to the difference of OM and mineral composition within the shale (Li et al., 2015; Chen et al., 2021). The methane adsorption isotherm of the dry shale samples showes a trend of increasing and then decreasing with pressure increasing, as shown in Fig. 12(a). When pressure is increased in the low-pressure stage (0–5 MPa), the methane adsorption rises sharply and almost linearly. In the intermediate stage (0–11 MPa), the excess methane adsorption increases slowly and reaches a maximum at 11 Mpa. Additionally, in the high-pressure stage, the adsorption capacity is saturated as the methane molecules in the adsorption layer gradually increase to saturation, with further pressure increases the excess adsorption gradually decreases. As illustrated in Fig. 12(b) and (c), in

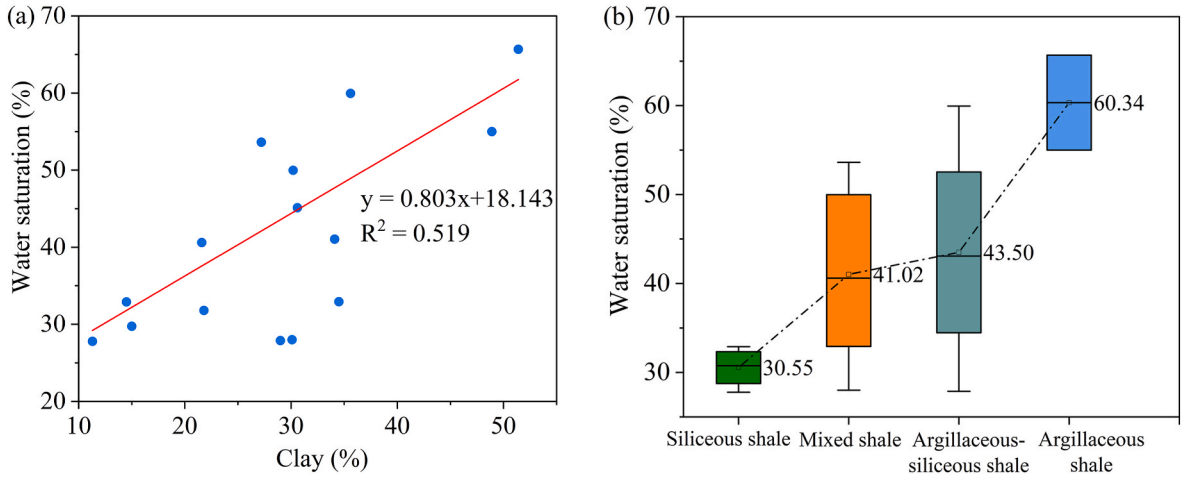

Fig. 11. (a) Correlation between water saturation and clay content; (b) Water saturation of various shale lithofacies.

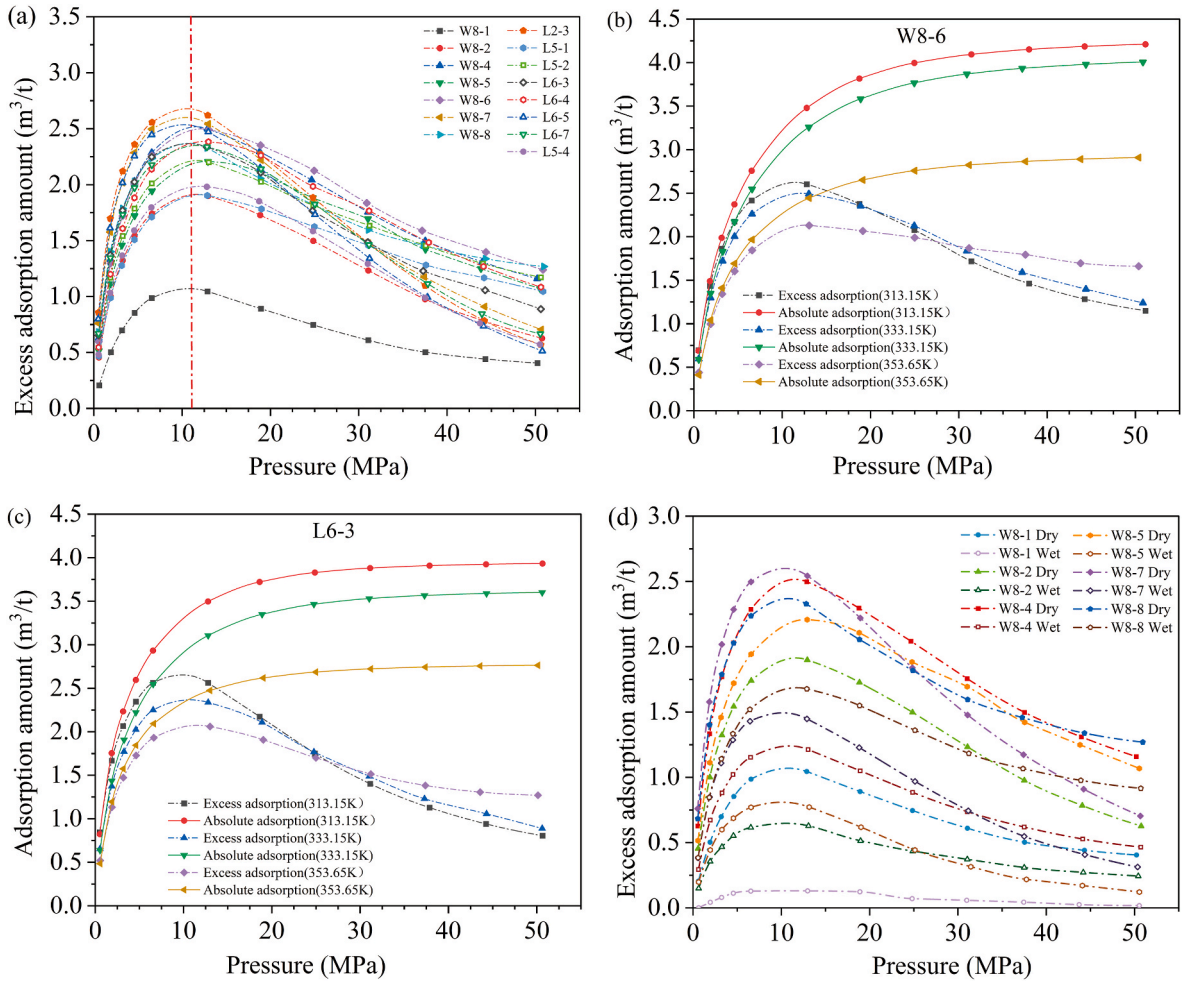

Fig. 12. Characteristics of high-pressure methane adsorption. (a) Isotherms of dry sample excess methane adsorption at 333.15 K. (b) Comparison between excess and absolute adsorption isotherms in the dry shale sample W8-6 at 313.15 K, 333.15 K and 353.65 K. (c) Comparison between excess and absolute adsorption isotherms in the dry shale sample L6-3 at 313.15 K, 333.15 K and 353.65 K. (d) Isotherms of dry and wet samples excess methane adsorption at 333.15 K.

the low-pressure stage, the rate of increase in methane adsorption decreases with higher temperatures, and the maximum methane excess adsorption decreases with higher temperatures. In the high-pressure stage, the rate of decrease in excess adsorption decreases at lower temperatures. As depicted in Fig. 12(d), wet shale samples exhibit substantially less excess adsorption than dry samples, indicating that water takes up the adsorption sites in the pores and significantly reduces the shale adsorption capacity. This result agrees with Wang et al. and Zou et al. (Wang and Yu, 2016; Zou et al., 2018).

5.4.2. *Evaluation of supercritical adsorption models*

The supercritical excess adsorption models such as S-L, S-BET, S-DA, S-DR and Ono-Kondo were selected and combined with experimental data on supercritical methane adsorption to obtain the values of parameters to be determined in each model via the Levenberg-Marquardt (LM) optimisation algorithm in Origin software. The above five models' fitted correlation coefficients (R^2) were greater than 0.95, indicating a very well fit, as listed in Table 4. Typical W8-8 sample was selected and the fit results of the S-L, S-BET, S-DA, S-DR and Ono-Kondo models were compared and analysed, as illustrated in Fig. 13. The results reveal that all models fits the measured data well at the low pressure stage, while the S-L and S-DR models differ significantly from the measured data at the high pressure stage and are not as well suited; the predicted values of the S-DA and Ono-Kondo models differ little from the measured data throughout the whole pressure stage. However, the adsorbed gas density of many shale samples fitted by the Ono-Kondo model exceed the 0.424 g/cm^3 and thus lose its actual physical significance. As shown in Fig. 14 and Table 4, the adsorbed gas density obtained from the S-L, S-BET, S-DA and S-DR models did not exceed 0.424 g/cm^3 (except for the experimental results of the W8-6 sample at 80.5 °C); all of them were consistent with the thermodynamic properties of methane in the supercritical conditions and the fitting results were reliable.

To further evaluate each excess adsorption model's efficacy and applicability, the root mean square error (RMSE) is introduced to assist in the determination. A smaller RMSE value suggests that the model fits better, and the RMSE is calculated as follows:

$$RMSE = \sqrt{\frac{1}{N-K}\sum_{i=1}^{N}(V_e - V_m)^2} \tag{23}$$

where *RMSE* is the root mean square error; N is the number of observations; K is the number of fitted parameters; V_e is measured data; V_m is modeling data.

The RMSE values of the S-L, S-BET, S-DA and S-DR models are shown in Table 4 and Fig. 15. The RMSE values of the S-L model range from 0.0280 to 0.0861, with an average of 0.0556, which is significantly higher than the rest of the models, indicating that S-L model predictions are poor. The RMSE values of S-BET model vary between 0.0138 and 0.0784, averaging 0.0478; and mean RMSE values of S-DR model is 0.0384. The RMSE values of the S-DA model are generally small, ranging from 0.0139 to 0.0547, with a minimum average of 0.024. The S-DA model predictions deviated less from the measured data throughout the

Table 4
Fitting parameters of different models for supercritical methane excess adsorption on the Wufeng-Longmaxi Shale samples
Continued Table 4. Fitting parameters of different models for supercritical methane excess adsorption on the Wufeng-Longmaxi Shale samples.

Models	Parameters	Sample ID								
		W8-1	W8-2	W8-4	W8-5	W8-7	W8-8	W8-6(40 °C)	W8-6(60 °C)	W8-6(80.5 °C)
S-L	V_L (m^3/t)	1.8552	3.5883	4.2332	4.0189	4.2847	3.3636	4.4587	4.3551	3.2282
	P_L (MPa)	4.5898	4.9292	4.0026	5.0567	3.0566	2.4228	3.8137	4.3979	4.1105
	ρ_{ads} (g/cm^3)	0.3103	0.3058	0.3488	0.3533	0.2996	0.3963	0.3624	0.3592	0.5108
	R^2	0.9849	0.9940	0.9933	0.9895	0.9943	0.9882	0.9855	0.9931	0.9967
	RMSE	0.0349	0.0400	0.0557	0.0556	0.0566	0.0702	0.0516	0.0280	0.0349
S-BET	k_1	0.0177	0.0074	0.0051	0.0065	0.0038	0.0042	0.0048	0.0055	0.0071
	k_2	0.3938	0.3253	0.2660	0.3054	0.2596	0.3026	0.2614	0.2646	0.3143
	k_3	1.8454	−0.3654	−0.2668	−0.5392	−0.2269	−0.0095	−0.3039	−0.3088	0.1619
	ρ_{ads} (g/cm^3)	0.3823	0.2938	0.3278	0.3115	0.2899	0.3997	0.3368	0.3317	0.6208
	R^2	0.9979	0.9960	0.9949	0.9953	0.9959	0.9886	0.9882	0.9952	0.9966
	RMSE	0.0138	0.0349	0.0399	0.0507	0.0592	0.0632	0.0451	0.0284	0.0138
S-DA	V_M (m^3/t)	1.5208	3.2914	3.9801	3.8831	4.0581	3.1356	4.2708	4.0787	2.9900
	D	0.0544	0.1493	0.1042	0.1631	0.0917	0.0330	0.1185	0.1150	0.0443
	n	2.4429	1.7148	1.871	1.6329	1.9156	2.4468	1.771	1.8246	2.3264
	ρ_{ads} (g/cm^3)	0.3234	0.3042	0.3460	0.3444	0.2976	0.4023	0.3569	0.3556	0.5242
	R^2	0.9896	0.9994	0.9992	0.9994	0.9997	0.9902	0.9978	0.9992	0.9962
	RMSE	0.0307	0.0139	0.0146	0.0141	0.0547	0.0271	0.0185	0.0302	0.0307
S-DR	V_M (m^3/t)	1.6450	3.0597	3.8571	3.4879	3.9874	3.3921	4.0309	3.8993	3.2223
	D	0.1004	0.0988	0.0855	0.0926	0.0809	0.0669	0.0833	0.0878	0.0770
	ρ_{ads} (g/cm^3)	0.3121	0.3129	0.3519	0.3642	0.2996	0.3797	0.3672	0.3647	0.4813
	R^2	0.9835	0.9962	0.9986	0.9946	0.9995	0.9842	0.9957	0.9981	0.9946
	RMSE	0.0365	0.0317	0.0401	0.0174	0.0655	0.0384	0.0266	0.0359	0.0365
Ono-Kondo	V_0 (m^3/t)	1.1238	2.14423	2.3191	2.1825	2.5047	1.7766	2.4251	2.3519	2.0356
	ε_s/k	−854.590	−838.221	−1003.71	−944.705	−981.227	−1233.600	−1011.065	−992.981	−1000
	ρ_{ads} (g/cm^3)	0.4386	0.4365	0.5339	0.5469	0.4283	0.6329	0.55315	0.5568	0.6892
	R^2	0.9964	0.9813	0.9861	0.9789	0.9810	0.9900	0.97264	0.9858	0.9751

Models	Parameters	Sample ID									
		L2-3	L5-1	L5-2	L6-4	L6-5	L6-7	L5-4	L6-3(40 °C)	L6-3(60 °C)	L6-3(80.5 °C)
S-L	V_L (m^3/t)	4.4535	3.1512	3.5601	4.3782	4.1926	4.3165	3.9684	4.1288	3.8644	3.0614
	P_L (MPa)	2.9654	4.1053	3.7496	5.014	2.8650	4.2267	5.4699	2.5669	3.2586	2.9964
	ρ_{ads} (g/cm^3)	0.2879	0.3875	0.3819	0.3426	0.2855	0.298	0.2956	0.3261	0.3254	0.3932
	R^2	0.977	0.9927	0.9948	0.9927	0.9898	0.983	0.9877	0.99	0.9932	0.9888
	RMSE	0.0892	0.0382	0.0371	0.0512	0.0782	0.0861	0.0622	0.0728	0.0504	0.0495
S-BET	k_1	0.0033	0.0071	0.0059	0.0060	0.0035	0.0048	0.0069	0.0037	0.0047	0.0055
	k_2	0.2673	0.3589	0.3066	0.2746	0.2769	0.2907	0.3214	0.2647	0.2791	0.3262
	k_3	−0.3937	−0.4068	−0.222	−0.4161	−0.3479	−0.5092	−0.554	−0.139	−0.1585	0.071
	ρ_{ads} (g/cm^3)	0.2727	0.3513	0.3626	0.3121	0.2735	0.2778	0.2783	0.3198	0.3179	0.4092
	R^2	0.9941	0.9945	0.9954	0.9964	0.9940	0.9919	0.9943	0.9908	0.9939	0.9900
	RMSE	0.0654	0.0353	0.0370	0.0382	0.0639	0.0634	0.0450	0.0784	0.0511	0.0495
S-DA	V_M	4.4249	3.0040	3.3229	4.1126	4.1142	4.2987	3.7951	3.9454	3.6230	2.7851
	D	0.1277	0.1007	0.0777	0.1469	0.1145	0.1896	0.2185	0.0758	0.0827	0.0329
	n	1.6833	1.877	2.0258	1.7053	1.7504	1.5068	1.4810	1.9804	1.9843	2.5055
	ρ_{ads} (g/cm^3)	0.2822	0.3818	0.3819	0.3382	0.2811	0.2903	0.2901	0.3237	0.3243	0.4062
	R^2	0.9997	0.9990	0.9984	0.9995	0.9998	0.9991	0.9995	0.9972	0.9980	0.9890
	RMSE	0.0145	0.0148	0.0216	0.0146	0.0123	0.0216	0.0132	0.0413	0.0289	0.0519
S-DR	V_M (m^3/t)	4.1153	2.9116	3.3428	3.792	3.8956	3.7472	3.2559	3.9301	3.6109	3.0567
	D	0.0798	0.0829	0.0809	0.094	0.0792	0.0912	0.1029	0.0736	0.0808	0.0732
	ρ_{ads} (g/cm^3)	0.2888	0.3896	0.3804	0.3522	0.2860	0.3041	0.3052	0.3242	0.3248	0.3763
	R^2	0.9965	0.9985	0.9984	0.9963	0.9978	0.9895	0.9884	0.9971	0.998	0.982
	RMSE	0.0475	0.0172	0.0205	0.0364	0.0362	0.0677	0.0604	0.0390	0.0273	0.0627
Ono-Kondo	V_0 (m^3/t)	2.6437	1.6631	1.8908	2.4233	2.5052	2.5676	2.4275	2.7871	2.6482	1.6177
	ε_s/k	−964.32	−1062.69	−1080.39	−922.767	−966.282	−875.389	−784.3	−917.48	−867.947	−1189.06
	ρ_{ads} (g/cm^3)	0.4057	0.6209	0.6068	0.5205	0.4000	0.424	0.416	0.424	0.424	0.6348
	R^2	0.9643	0.9874	0.9909	0.9827	0.9691	0.96	0.9672	0.9647	0.9659	0.9923

whole pressure phase and fitted the best, as illustrated in Figs. 13 and 15. Thus, the excess adsorption of supercritical methane is mainly characterized by the S-DA model in this study.

5.4.3. Comparison of absolute and excess adsorption amount

The absolute adsorption isotherm can be derived from the measured excess adsorption data by using the methane density of adsorbed phase and Eq. (9). As shown in Fig. 12b and c, the absolute adsorption amount is always larger than that of excess adsorption and the difference is more significant under high pressure. This finding suggests that the measured excess adsorption amount should be corrected to the absolute adsorption amount, otherwise the content of adsorbed gas will be seriously underestimated (Dang et al., 2020; Zhou et al., 2018).

5.5. Controlling factors of shale adsorption capacity

5.5.1. Effects of TOC and mineral compositions on adsorption capacity

Its own TOC, mineral composition, pore structure parameters and original water content play a significant role in the shale's methane adsorption capacity (Chalmers and Bustin, 2008; Zhou et al., 2019; Chen et al., 2021). As illustrated in Fig. 16, the maximum shale methane adsorption capacity and TOC content are closely correlated, with a Pearson coefficient (r) of 0.82, and increases gradually as the TOC content increases. This reveals that TOC content is crucial for shale

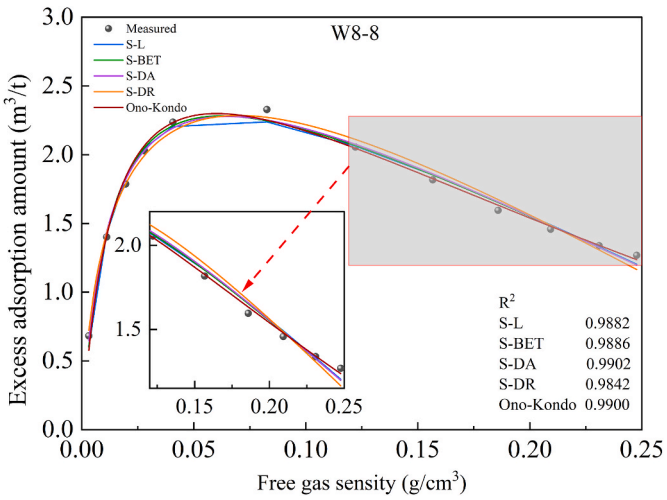

Fig. 13. Comparison of modeling results for excess methane adsorption by S-L, S-BET, S-DA, S-DR and Ono-Kondo models on shale sample W8-8.

methane adsorption capacity. In addition, the TOC content correlates well with the micropore volume, SSA of micropore and total SSA, with a Pearson coefficient r of 0.73, 0.77 and 0.86, respectively. The fact is that high TOC content facilitates the development of abundant OM pores, which have a large SSA and further provide abundance adsorption sites for methane molecules. Meanwhile, the precence of polar functional groups in OM also enhance its adsorption capacity (Yang et al., 2015; Zhang et al., 2012).

As demonstrated in Fig. 16, the maximum methane adsorption correlates weakly with quartz (r = 0.41), mainly due to quartz being associated with the development of meso-macropores which provide a small SSA. Thus, quartz is not a key factor affecting the shale adsorption capacity. Clay minerals with large SSA have a positive impact on shale adsorption capacity due to their abundance of adsorption sites (Lu et al., 1995; Heller and Zoback, 2014). However, without taking into account the OM obscuring the role of clay minerals in the adsorption capacity, a negative correlation was found between the two, with a correlation coefficient r of −0.47, Fig. 16. To avoid high TOC content obscuring the role of clay minerals, then the maximum methane adsorption was normalized to the per unit TOC content (1%) and clay mineral content and shale methane adsorption capacity exhibited a good positive correlation(r = 0.70), as shown in Fig. 17. This reveals that clay minerals do, to a certain extent, contribute to the adsorption capacity of shale.

5.5.2. *Effects of pore structure parameter on adsorption capacity*

Previous studies reported that the shale adsorption capacity and pore structure is closely related (Wang et al., 2016b; Yang et al., 2016; Ma et al., 2020; Xu et al., 2020a). The correlation coefficients between maximum methane adsorption and micropore volume and total PV are 0.73 and 0.61 respectively, thus indicating that micropore volume is a crucial factor in controlling methane adsorption capacity, Fig. 16. The reason is that micropores provide a large SSA, which in turn provides abundant methane adsorption sites. Over 75% of the SSA in the Wufeng-Longmaxi Shale is contributed by micropores, as was explained in section 5.2.5. Therefore, the methane adsorption capacity is mainly controlled by micropores, while non-micropores mainly accommodate free gas. In addition, the correlation coefficients between maximum methane adsorption and micropore SSA and total SSA are 0.77 and 0.86 respectively, indicating that the maximum methane adsorption correlates better with total SSA than it does with micropores. Adsorption capacity is, in fact, mostly correlated with total SSA, with mesopores and macropores in addition to micropores also providing part of the total SSA.

5.5.3. *Effects of water and temperature on adsorption capacity*

Water can lead to a reduction in shale methane adsorption capacity (Wang and Yu, 2016; Zou et al., 2018, 2019; Chen et al., 2021a). However, previous methane adsorption experiments on wet shale samples have typically been carried out under water equilibrium conditions, which differ from actual in situ reservoir water conditions (Yang et al., 2017a; Zou et al., 2019). In this study, the water saturation of core samples under in situ reservoir conditions was restored, followed by high temperature and pressure methane adsorption experiments. The percentage reduction in maximum methane adsorption increases with water saturation because of water occupying the adsorption sites of pores in the shale (Wang and Yu, 2016; Yang et al., 2017a; Feng et al., 2018), with the adsorption capacity of water-bearing shales decreasing by 28%~81% at a water saturation of 30%~65% compared to dry shales, as shown in Fig. 18(a). Furthermore, the maximum methane adsorption is significantly negatively correlated with temperature, with

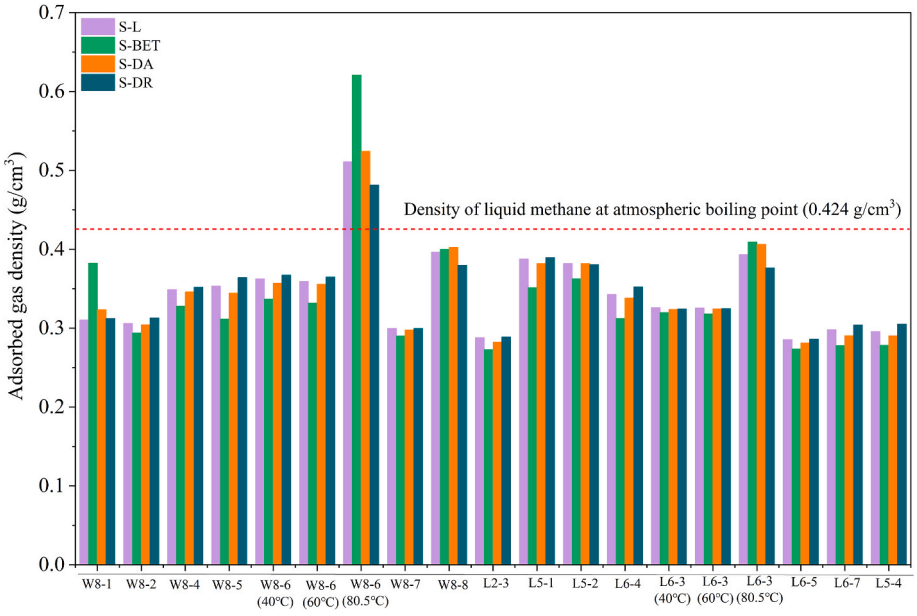

Fig. 14. Comparison of the ρ_{ads} fitted by different models.

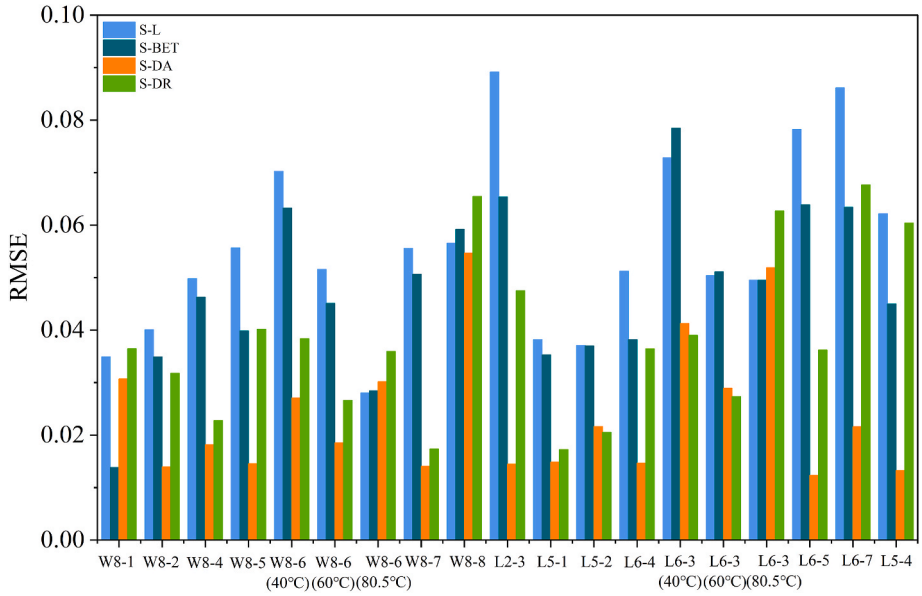

Fig. 15. Comparison of the RMSE values calculated from different models.

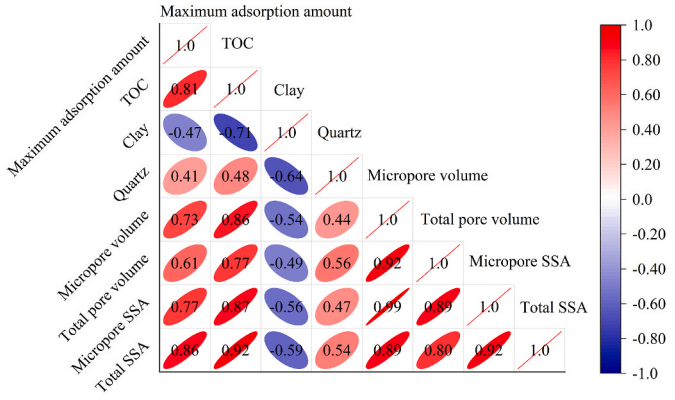

Fig. 16. Pearson correlation coefficients of shale maximum adsorption amount, TOC, Clay, Quartz, and pore structure parameters.

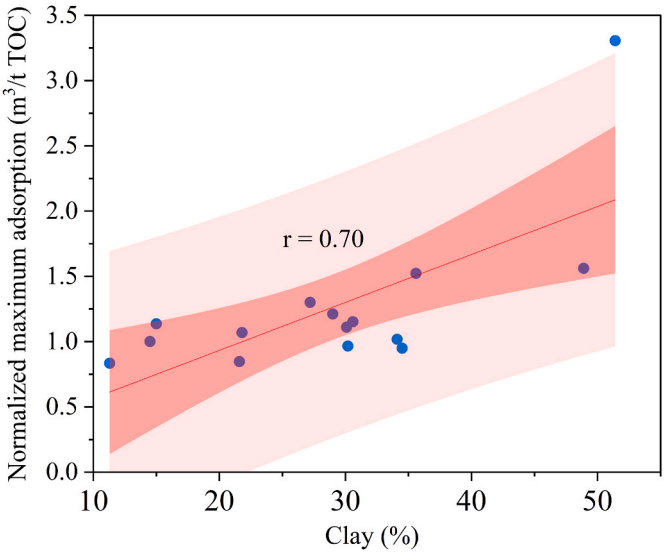

Fig. 17. The correlation between normalized maximum adsorption amount and clay minerals.

fitted correlation coefficients R^2 all exceeding 0.85, indicating that temperature has an inhibitory activity on the shale methane adsorption capacity, Fig. 18(b). As the temperature increased from 40 °C to 80 °C, the methane adsorption capacity decreased from 3.95 to 2.79 m^3/t, a 29% decrease. This reason is that temperature rising of the adsorption system increases the potential energy of methane molecular and facilitates the desorption of adsorbed methane to the free state, thus weakening the shale methane adsorption capacity (Wu et al., 2016; Chen et al., 2018; Zou et al., 2019; Li et al., 2020, 2021).

5.6. Shale gas occurrence and content of different shale lithofacies

5.6.1. Gas-in-place estimation

Combining the results of methane adsorption experiments on the sample L2-3 with the adsorbed and free gas content prediction model (Eq. (15) and (22)) will yield the in-situ shale reservoir's adsorbed and free gas content. The average reservoir pressure gradient, surface temperature and temperature gradient were set to 18 MPa/km, 30 °C and 25 °C/km, respectively. Moreover, the reservoir porosity, rock density, and water saturation were set at 6.0%, 2.5 g/cm^3, and 0% respectively; and these parameters did not vary with the depth of burial.

The absolute adsorption amount increases rapidly with the depth of burial and then decreases slowly due to the dominant effect of pressure on shale methane adsorption at shallow burial depths, where pressure increases leading to a sharp increase in adsorption, as demonstrated in Fig. 19(a). However, the effect of pressure is weaker at deeper burial depths, and the adsorption capacity is significantly influenced by temperature, which slowly decreases with increasing temperature. With increasing burial depth, the content of both actual free gas (with adsorbed phase volume correction) and total gas both increase, rapidly at shallow depths and slowly at deeper depths. The adsorbed gas dominates at shallow depths, accounting for over 80% of the total. Then the proportion of adsorbed gas and free gas is equal (about 1200 m) as burial depth increasing, and free gas dominates at deeper burial depths, with over 90% at 5000 m, as illustrated in Fig. 19(b).

5.6.2. Shale gas occurrence of different lithofacies and implication for shale gas exploration and development

Adsorbed gas and free gas account for the majority of shale gas, while dissolved gas is negligible (Curtis, 2002; Feng et al., 2020; Gou et al.,

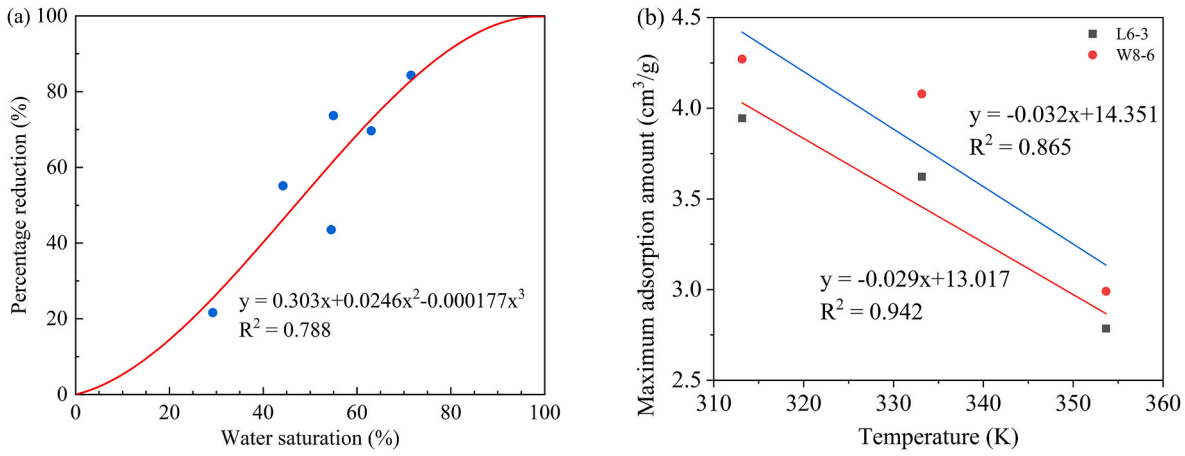

Fig. 18. (a) Correlation between the percentage reduction of maximum adsorption and water saturation; (b) The correlation between temperature and the maximum amount of adsorption.

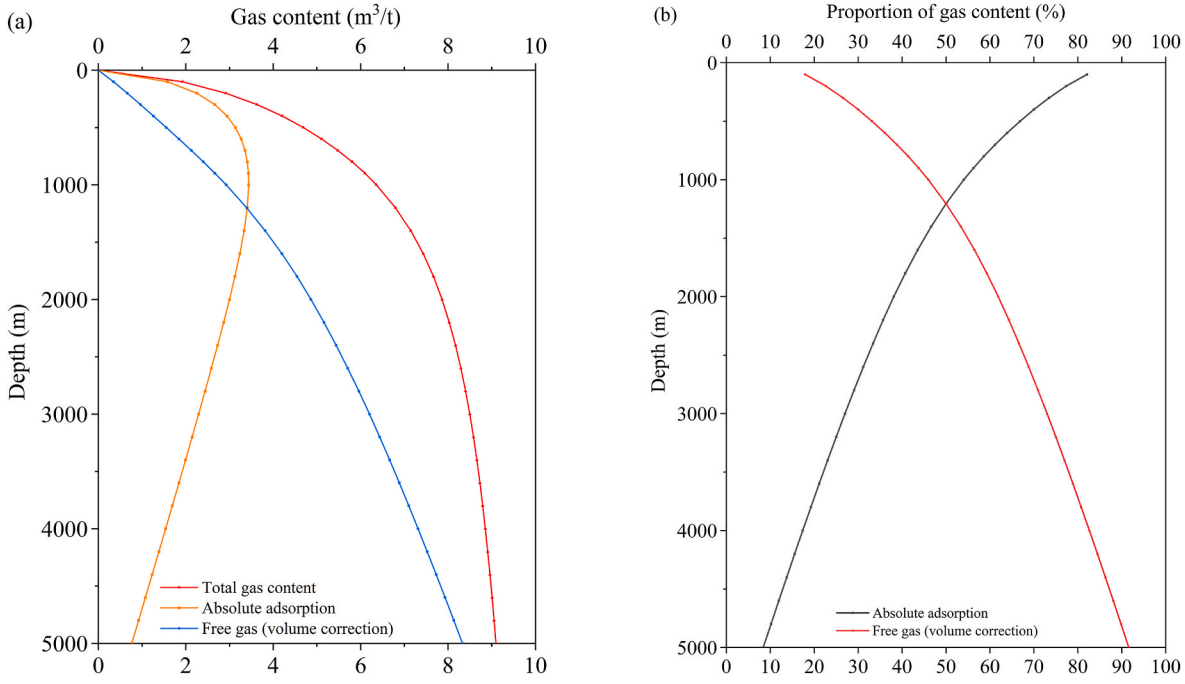

Fig. 19. (a) In-situ shale reservoir gas content with burial depth; (b) Proportion of gas content with burial depth.

2020). As discussed above, the content of adsorbed gas is mainly determined by the OM content and the content of free gas is controlled by porosity. However, the occurrence of moisture can severely reduce the content of both adsorbed and free gases. Based on the above characteristics of mineral compositions, TOC content, pore structure, and water saturation of various shale lithofacies, and free gas are dominated at deep shale, then the pattern of shale gas occurrence and gas content in different lithofacies are summarised.

Fig. 20(a) shows the pattern of shale gas occurrence and content in siliceous shale. The adsorbed methane molecules are mainly adsorbed on the surface of OM pores, calcite and clay minerals. Due to its high TOC content and abundant OM pores, the content of adsorbed gas is largest among four lithofacies. Meanwhile, it also possesses the highest siliceous content, forming and perserving an abundance of interP and intraP pores due to a strong resistance to compaction, and the free gas is mainly found in interP and intraP pores of quartz, feldspar and calcite minerals and in OM macropores. The lowest water saturation of 30% is in siliceous shale and the water is mainly in the pores of the clay minerals.

The pattern of shale gas occurrence and content of mixed shale is shown in Fig. 20(b), the adsorbed gas content is high due to its high OM content and the abundant OM pores. In addition, the intraP pores associated with acid fluid dissolution are abundant due to its relative high content of carbonate such as calcite and dolomite, which provide storage space for free gas. However, the water saturation of the mixed shale increases to 40%, with water mainly occupying the pores associated with clay minerals and interP pores forming by the quartz and carbonate minerals, and its gas content is reduced compared to the siliceous shale.

Fig. 20(c) shows the pattern of shale gas occurrence and content in argillaceous-siliceous shale. Compared with siliceous shale, its TOC content is slightly lower, resulting in reduced OM pore number and adsorbed gas content. In addition, the clay mineral content increases, the total reservoir porosity decreases as well as the water saturation increased to 45%, leading in a significant decrease in free gas content.

The pattern of shale gas occurrence and content of argillaceous shale

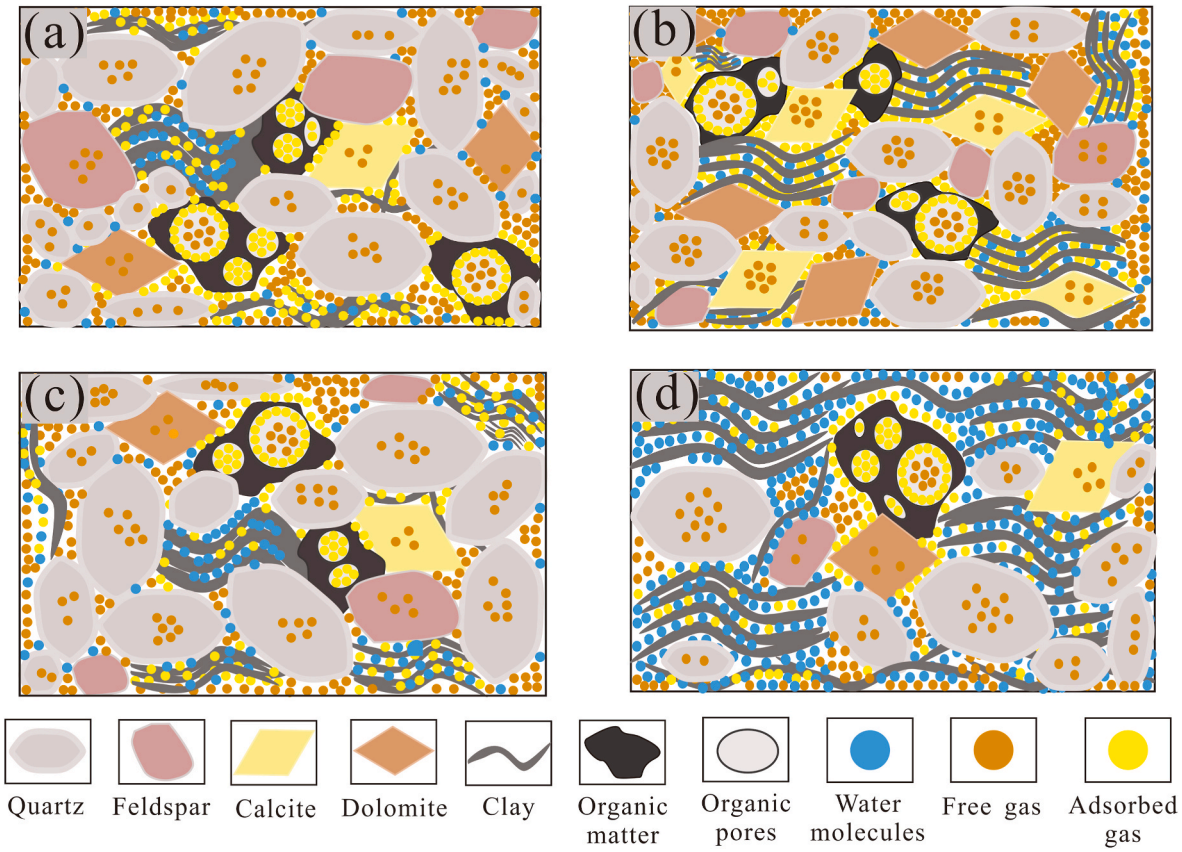

Fig. 20. Pattern diagram of shale gas occurrence and content of different shale lithofacies. (a) Siliceous shale; (b) Mixed shale; (c) Argillaceous-siliceous shale; (d) Argillaceous shale.

Table 5
Adsorbed and free gas contents of various shale lithofacies.

Lithofacies	TOC (%)	Porosity (%)	Water saturation (%)	Gas content (m^3/t)		
				Absolute adsorbed gas	Free gas (volume correction)	Total
SS	4.00	6.0	30.0	1.43	4.39	5.82
MS	3.50	5.0	40.0	0.97	3.19	4.16
A-SS	3.00	4.5	45.0	0.71	2.69	3.40
AS	2.00	3.5	60.0	0.23	1.65	1.88

is demonstrated in Fig. 20(d), the adsorbed gas content is minimum due to its lowest OM content and OM pores among four lithofacies. However, argillaceous shale possess the highest clay content and water saturation up to 60%, with water occupying the pores associated with clay minerals and interP pores forming by the quartz and feldspar, leading to a significant reduction in free gas content as well.

The gas content of the different lithofacies reservoirs were calculated by combining the pattern of shale gas occurrence, the adsorbed and free gas content prediction model, and geological parameters including TOC content, porosity and water saturation of different lithofacies. As listed in Table 5, the content of both adsorbed and free gas are largest in the siliceous shale, with 1.43 m^3/t and 4.39 m^3/t, respectively; and followed by the mixed and argillaceous-siliceous shale. However, the argillaceous shale possesses the lowest gas content, with adsorbed and free gas contents of 0.23 m^3/t and 1.65 m^3/t respectively. It is estimated that siliceous shale has a three-fold higher gas content than argillaceous shale. In summary, siliceous shale and mixed shale are favorable reservoirs for shale gas exploration and development due to their high gas contents and low water saturation.

6. Conclusions

In this study, FE-SEM and LPGA (CO_2 and N_2) experiments were used to fully characterize and clarify the differences in the pore structure characteristics of various lithofacies. The water content of the actual in-situ shale reservoir is restored according to the amount of moisture adsorbed at different relative humidities. Shale adsorption capacity was investigated by high temperature and pressure methane adsorption experiments and characterized by supercritical excess adsorption S-L, S-BET, S-DA, S-DR and Ono-Kondo models. In addition, the correlation between shale adsorption capacity and TOC content, mineral composition, pore structure parameters and water saturation were also analysed. Finally, the pattern of shale gas occurrence and content in various lithofacies are summarised. The main conclusions are summarised as follows:

(1) The mineral compositions identified four shale lithofacies in the Wufeng–Longmaxi Shale. Pores are abundant in siliceous shale and mixed shale, with organic pores accounting for over 45%, while argillaceous-siliceous and argillaceous shale are dominated by inorganic pores, accounting for over 70%. The largest PV and

SSA are in siliceous shale, averaging 0.0310 cm^3/g and 25.827 m^2/g, respectively. The PV and SSA are lowest in argillaceous shale, averaging 0.0217 cm^3/g and 18.734 m^2/g, respectively. Mesopores account for over 60% of the shale PV and micropores provide over 75% of the total SSA.

(2) The S-DA excess adsorption model predictions deviated less from the measured data among above five models. The shale adsorption capacity is dominated by TOC content and total SSA, and clay minerals do, to a certain extent, contribute to the adsorption capacity of shale. However, water and temperature have an inhibitory activity on adsorption capacity, with the adsorption capacity of water-bearing shales decreasing by 28%~81% at a water saturation of 30%~65% compared to dry shales. As the temperature increased from 40 °C to 80 °C, the methane adsorption capacity decreased from 3.95 to 2.79 m^3/t, a 29% decrease.

(3) The absolute adsorption amount increases rapidly with the depth of burial and then decreases slowly. And the content of both the actual free gas (with adsorbed phase volume correction) and total gas increase rapidly at shallow depths and then stabilizes slowly. Deep shale gas reservoirs are dominated by free gas, accounting for over 90% at 5000 m.

(4) Siliceous shale has the highest gas content, followed by mixed shale, argillaceous-siliceous shale, and argillaceous shale. It is estimated that siliceous shale has a three-fold higher gas content than argillaceous shale. In summary, siliceous and mixed shale are favorable reservoirs for shale gas exploration and development due to their high gas contents and low water saturation.

Author contributions

Chao Qian: Conceptualization, Methodology, Software, Writing original draft. Xizhe Li: Funding acquisition and Supervision. Qing Zhang: Resources and Writing - review & editing. Weijun Shen: Supervision and Writing - review & editing. Wei Guo: Resources. Wei Lin: Investigation and Writing - review & editing. Lingling Han: Investigation. Yue Cui: Investigation and Validation. Yize Huang: Investigation and Validation. Xiangyang Pei: Investigation and Formal analysis. Zhichao Yu: Investigation and Formal analysis.

Author information

Chao Qian - Shale Gas Exploration and Development Department, CNPC Chuanqing Drilling Engineering Co., Ltd., Chengdu, Sichuan 610051, China; Research Institute of Petroleum Exploration and Development, PetroChina, Beijing 100083, China; **Xizhe Li -** Research Institute of Petroleum Exploration and Development, PetroChina, Beijing 100083, China; **Qing Zhang** - Shale Gas Exploration and Development Department, CNPC Chuanqing Drilling Engineering Co., Ltd., Chengdu, Sichuan 610051, China; **Weijun Shen** - Key Laboratory for Mechanics in Fluid Solid Coupling Systems, Institute of Mechanics, Chinese Academy of Sciences, Beijing 100190, China; School of Engineering Science, University of Chinese Academy of Sciences, Beijing 100049, China; **Wei Guo** - Research Institute of Petroleum Exploration and Development, PetroChina, Beijing100083, China; **Wei Lin -** School of Geosciences, Yangtze University, Wuhan 430100, China; **Lingling Han-** Institute of Porous Flow and Fluid Mechanics, Chinese Academy of Sciences, Langfang, Hebei 065007, China ; **Yue Cui -** Institute of Porous Flow and Fluid Mechanics, Chinese Academy of Sciences, Langfang, Hebei 065007, China; **Yize Huang -** Institute of Porous Flow and Fluid Mechanics, Chinese Academy of Sciences, Langfang, Hebei 065007, China; **Xiangyang Pei -** Research Institute of Petroleum Exploration and Development, PetroChina, Beijing 100083, China; **Zhichao Yu -** College of Geosciences, China University of Petroleum, Beijing 102249, China.

Declaration of competing interest

The authors declare that there are no conflicts of interest regarding the publication of this paper.

Data availability

Data will be made available on request.

Acknowledgments

This work was supported by the National Natural Science Foundation of China (nos 11802312 and U1762216) and Hubei Provincial Natural Science Foundation of China (Grant No. 2021CFB182). Many thanks to the BeiShiDe instruments.

Appendix A. Supplementary data

Supplementary data associated with this article can be found, in the online version, at https://doi.org/10.1016/j.geoen.2023.211701.

References

Ambrose, R.J., Hartman, R.C., Diaz-Campos, M., Akkutlu, I.Y., Sondergeld, C.H., 2012. Shale gas-in-place calculations Part I: new pore-scale considerations. SPE J. 17, 219–229.

Astakhov, V.A., Dubinin, M.M., 1971. Development of the concept of volume filling of micropores in the adsorption of gases and vapors by microporous adsorbents. Russ. Chem. Bull. 20, 13–16.

Bi, H., Jiang, Z., Li, J., Xiong, F., Li, P., Chen, L., 2017. Ono–kondo model for supercritical shale gas storage: a case study of silurian longmaxi shale in southeast chongqing, China. Energy Fuel. 31, 2755–2764.

Borjigin, T., Shen, B., Yu, L., Yang, Y., Zhang, W., Tao, C., Xi, B., Zhang, Q., Bao, F., Qin, J., 2017. Mechanisms of shale gas generation and accumulation in the ordovician Wufeng-Longmaxi Formation, Sichuan Basin, SW China. Petrol. Explor. Dev. 44, 69–78.

Brunauer, S., Emmett, P.H., Teller, E., 1938. Adsorption of gases in multimolecular layers. J. Am. Chem. Soc. 60, 309–319.

Chalmers, G.R.L., Bustin, R.M., 2008. Lower Cretaceous gas shales in northeastern British Columbia, Part I: geological controls on methane sorption capacity. Bull. Can. Petrol. Geol. 56, 1–21.

Chalmers, G.R., Bustin, R.M., Power, I.M., 2012. Characterization of gas shale pore systems by porosimetry, pycnometry, surface area, and field emission scanning electron microscopy/transmission electron microscopy image analyses: examples from the Barnett, Woodford, Haynesville, Marcellus, and Doig units. AAPG (Am. Assoc. Pet. Geol.) Bull. 96, 1099–1119.

Chandra, D., Vishal, V., 2021. A critical review on pore to continuum scale imaging techniques for enhanced shale gas recovery. Earth Sci. Rev. 217, 103638.

Chareonsuppanimit, P., Mohammad, S.A., Robinson, R.L., Gasem, K.A.M., 2012. High-pressure adsorption of gases on shales: measurements and modeling. Int. J. Coal Geol. 95, 34–46.

Charoensuppanimit, P., Mohammad, S.A., Gasem, K.A.M., 2016. Measurements and modeling of gas adsorption on shales. Energy Fuel. 30, 2309–2319.

Chen, L., Jiang, Z., Liu, K., Gao, F., 2017. Quantitative characterization of micropore structure for organic-rich Lower Silurian shale in the Upper Yangtze Platform, South China: implications for shale gas adsorption capacity. Advances in Geo-Energy Research 1, 112–123.

Chen, M., Kang, Y., Zhang, T., Li, X., Wu, K., Chen, Z., 2018. Methane adsorption behavior on shale matrix at in-situ pressure and temperature conditions: measurement and modeling. Fuel 228, 39–49.

Chen, L., Jiang, Z., Liu, Q., Jiang, S., Liu, K., Tan, J., Gao, F., 2019. Mechanism of shale gas occurrence: insights from comparative study on pore structures of marine and lacustrine shales. Mar. Petrol. Geol. 104, 200–216.

Chen, G., Li, C., Lu, S., Guo, T., Wang, M., Xue, Q., Zhang, T., Li, Z., Sun, Y., Liu, J., Jiang, S., 2021. Critical factors controlling adsorption capacity of shale gas in Wufeng-Longmaxi formation, Sichuan Basin: evidences from both experiments and molecular simulations. J. Nat. Gas Sci. Eng. 88, 103774.

Chen, L., Jiang, Z., Jiang, S., Guo, S., Tan, J., 2021a. Effect of pre-adsorbed water on methane adsorption capacity in shale-gas systems. Front. Earth Sci. 9, 757705.

Chen, L., Liu, K., Jiang, S., Huang, H., Tan, J., Zuo, L., 2021b. Effect of adsorbed phase density on the correction of methane excess adsorption to absolute adsorption in shale. Chem. Eng. J. 420, 127678.

Clarkson, C.R., Solano, N., Bustin, R.M., Bustin, A.M.M., Chalmers, G.R.L., He, L., Melnichenko, Y.B., Radliński, A.P., Blach, T.P., 2013. Pore structure characterization of North American shale gas reservoirs using USANS/SANS, gas adsorption, and mercury intrusion. Fuel 103, 606–616.

Dang, W., Zhang, J., Nie, H., Wang, F., Tang, X., Wu, N., Chen, Q., Wei, X., Wang, R., 2020. Isotherms, thermodynamics and kinetics of methane-shale adsorption pair

under supercritical condition: implications for understanding the nature of shale gas adsorption process. Chem. Eng. J. 383, 123191.
Curtis, J.B., 2002. Fractured shale-gas systems. AAPG (Am. Assoc. Pet. Geol.) Bull. 86 (11), 1921–1938.
Dang, W., Jiang, S., Zhang, J., Li, P., Nie, H., Liu, Y., Li, F., Sun, J., Tao, J., Shan, C., Tang, X., Wang, R., Yin, Y., 2021. A systematic experimental and modeling study of water adsorption/desorption behavior in organic-rich shale with different particle sizes. Chem. Eng. J. 426, 130596.
Feng, D., Li, X., Wang, X., Li, J., Sun, F., Sun, Z., Zhang, T., Li, P., Chen, Y., Zhang, X., 2018. Water adsorption and its impact on the pore structure characteristics of shale clay. Appl. Clay Sci. 155, 126–138.
Feng, G., Zhu, Y., Chen, S., Wang, Y., Ju, W., Hu, Y., You, Z., Wang, G.G.X., 2020. Supercritical methane adsorption on shale over wide pressure and temperature ranges: implications for gas-in-place estimation. Energy Fuel. 34, 3121–3134.
Gasparik, M., Bertier, P., Gensterblum, Y., Ghanizadeh, A., Krooss, B.M., Littke, R., 2014. Geological controls on the methane storage capacity in organic-rich shales. Int. J. Coal Geol. 123, 34–51.
Gensterblum, Y., Merkel, A., Busch, A., Krooss, B.M., 2013. High-pressure CH4 and CO2 sorption isotherms as a function of coal maturity and the influence of moisture. Int. J. Coal Geol. 118, 45–57.
Gibbs, J.W., 1878. On the equilibrium of heterogeneous substances. Am. J. Sci. s3–16, 441–458.
Gou, Q., Xu, S., Hao, F., Yang, F., Zhang, B., Shu, Z., Zhang, A., Wang, Y., Lu, Y., Cheng, X., Qing, J., Gao, M., 2019. Full-scale pores and micro-fractures characterization using FE-SEM, gas adsorption, nano-CT and micro-CT: a case study of the Silurian Longmaxi Formation shale in the Fuling area, Sichuan Basin, China. Fuel 253, 167–179.
Gou, Q., Xu, S., Hao, F., Zhang, B., Shu, Z., Yang, F., Wang, Y., Li, Q., 2020. Quantitative calculated shale gas contents with different lithofacies: a case study of Fuling gas shale, Sichuan Basin, China. J. Nat. Gas Sci. Eng. 76, 103222.
Guo, X., Li, Y., Borjigen, T., Wang, Q., Yuan, T., Shen, B., Ma, Z., Wei, F., 2020. Hydrocarbon generation and storage mechanisms of deep-water shelf shales of ordovician Wufeng Formation–silurian Longmaxi Formation in Sichuan Basin, China. Petrol. Explor. Dev. 47, 204–213.
Han, W., Li, A., Memon, A., Ma, M., 2021. Synergetic effect of water, temperature, and pressure on methane adsorption in shale gas reservoirs. ACS Omega 6, 2215–2229.
Han, L., Li, X., Guo, W., Ju, W., Cui, Y., Liu, Z., Qian, C., Shen, W., 2022. Characteristics and dominant factors for natural fractures in deep shale gas reservoirs: a case study of the wufeng-longmaxi formations in Luzhou block, southern China. Lithosphere, 9662175.
Hao, F., Zou, H., Lu, Y., 2013. Mechanisms of shale gas storage: implications for shale gas exploration in China. AAPG (Am. Assoc. Pet. Geol.) Bull. 97 (8), 1325–1346.
Heller, R., Zoback, M., 2014. Adsorption of methane and carbon dioxide on gas shale and pure mineral samples. J. Unconvent. Oil and Gas Resour. 8, 14–24.
Hughes, J.D., 2013. A reality check on the shale revolution. Nature 494, 307–308.
Ji, W., Song, Y., Jiang, Z., Chen, L., Li, Z., Yang, X., Meng, M., 2015. Estimation of marine shale methane adsorption capacity based on experimental investigations of Lower Silurian Longmaxi formation in the Upper Yangtze Platform, south China. Mar. Petrol. Geol. 68, 94–106.
Langmuir, I., 1918. The adsorption of gases on plane surfaces of glass, mica and platinum. J. Am. Chem. Soc. 40 (9), 1361–1403.
Li, J., Yan, X., Wang, W., Zhang, Y., Yin, J., Lu, S., Chen, F., Meng, Y., Zhang, X., Chen, X., Yan, Y., Zhu, J., 2015. Key factors controlling the gas adsorption capacity of shale: a study based on parallel experiments. Appl. Geochem. 58, 88–96.
Li, J., Li, B., Ren, C., Yang, K., Zhang, Y., 2020. Characterization of methane adsorption behavior on wet shale under different temperature conditions. Energy Fuel. 34, 2832–2848.
Li, J., Li, B., Gao, Z., Zhang, Y., Wang, B., 2021. Adsorption behavior, including the thermodynamic characteristics of wet shales under different temperatures and pressures. Chem. Eng. Sci. 230, 116228.
Li, X., Jiang, Z., Jiang, S., Wang, S., Miao, Y., Wu, F., Cao, X., 2021. Synergetic effects of matrix components and diagenetic processes on pore properties in the Lower Cambrian shale in Sichuan Basin, South China. J. Nat. Gas Sci. Eng., 104072
Li, Q., Li, B., Mei, W., Liu, Y., 2022. Genesis and sources of natural gas in fold-and-thrust belt: the Middle Permian in the NW Sichuan Basin. Mar. Petrol. Geol. 140, 105638.
Lin, W., Li, X., Yang, Z., Lin, L., Xiong, S., Wang, Z., Wang, X., Xiao, Q., 2018. A new improved threshold segmentation method for scanning images of reservoir rocks considering pore fractal characteristics. Fractals 26, 1840003.
Liu, K., Ostadhassan, M., Kong, L., 2018. Multifractal characteristics of Longmaxi Shale pore structures by N2 adsorption: a model comparison. J. Petrol. Sci. Eng. 168, 330–341.
Loucks, R.G., Ruppel, S.C., 2007. Mississippian barnett shale: lithofacies and depositional setting of a deep-water shale-gas succession in the fort worth basin, Texas. AAPG (Am. Assoc. Pet. Geol.) Bull. 91 (4), 579–601.
Loucks, R.G., Reed, R.M., Ruppel, S.C., Jarvie, D.M., 2009. Morphology, genesis, and distribution of nanometer-scale pores in siliceous mudstones of the mississippian barnett shale. J. Sediment. Res. 79, 848–861.
Loucks, R.G., Reed, R.M., Ruppel, S.C., Hammes, U., 2012. Spectrum of pore types and networks in mudrocks and a descriptive classification for matrix-related mudrock pores. AAPG (Am. Assoc. Pet. Geol.) Bull. 96 (6), 1071–1098.
Lu, X.C., Li, F.C., Watson, A.T., 1995. Adsorption measurements in devonian shales. Fuel 74, 599–603.
Ma, X., Xie, J., 2018. The progress and prospects of shale gas exploration and development in southern sichuan basin, SW China. Petrol. Explor. Dev. 45, 172–182.
Ma, X., Li, X., Liang, F., Wan, Y., Shi, Q., Wang, Y., Zhang, X., Che, M., Guo, W., Guo, W., 2020. Dominating factors on well productivity and development strategies optimization in Weiyuan shale gas play, Sichuan Basin, SW China. Petrol. Explor. Dev. 47, 594–602.
Ma, Y., Ardakani, O.H., Zhong, N., Liu, H., Huang, H., Larter, S., Zhang, C., 2020. Possible pore structure deformation effects on the shale gas enrichment: an example from the Lower Cambrian shales of the Eastern Upper Yangtze Platform, South China. Int. J. Coal Geol. 217, 103349.
Mastalerz, M., Schimmelmann, A., Drobniak, A., Chen, Y., 2013. Porosity of Devonian and Mississippian New Albany Shale across a maturation gradient: insights from organic petrology, gas adsorption, and mercury intrusion. AAPG (Am. Assoc. Pet. Geol.) Bull. 97 (10), 1621–1643.
Nie, H., Jin, Z., Ma, X., Liu, Z., Lin, T., Yang, Z., 2017. Dispositional characteristics of ordovician Wufeng Formation and silurian Longmaxi Formation in Sichuan Basin and its adjacent areas. Petroleum Research 2, 233–246.
Pan, X., Wang, Z., Li, Q., Gao, J., Zhu, L., Liu, W., 2020. Sedimentary environments and mechanism of organic matter enrichment of dark shales with low TOC in the Mesoproterozoic Cuizhuang Formation of the Ordos Basin: evidence from petrology, organic geochemistry, and major and trace elements. Mar. Petrol. Geol. 122, 104695.
Pang, P., Han, H., Hu, L., Guo, C., Gao, Y., Xie, Y., 2021. The calculations of pore structure parameters from gas adsorption experiments of shales: which models are better? J. Nat. Gas Sci. Eng. 94, 104060.
Qi, Y., Ju, Y., Jia, T., Zhu, H., Cai, J., 2017. Nanoporous structure and gas occurrence of organic-rich shales. J. Nanosci. Nanotechnol. 17, 6942–6950.
Qian, C., Li, X., Shen, W., Zhang, Q., Guo, W., Hu, Y., Cui, Y., Jia, Y., 2022. Study on the pore structure and fractal characteristics of different lithofacies of wufeng–longmaxi Formation shale in southern Sichuan Basin, China. ACS Omega 7, 8724–8738.
Qiu, Z., Liu, B., Lu, B., Shi, Z., Li, Z., 2022. Mineralogical and petrographic characteristics of the Ordovician-Silurian Wufeng-Longmaxi Shale in the Sichuan Basin and implications for depositional conditions and diagenesis of black shales. Mar. Petrol. Geol. 135, 105428.
Rexer, T.F.T., Benham, M.J., Aplin, A.C., Thomas, K.M., 2013. Methane adsorption on shale under simulated geological temperature and pressure conditions. Energy Fuel. 27, 3099–3109.
Roshan, H., Ehsani, S., Marjo, C.E., Andersen, M.S., Acworth, R.I., 2015. Mechanisms of water adsorption into partially saturated fractured shales: an experimental study. Fuel 159, 628–637.
Ross, D.J.K., Marc Bustin, R., 2009. The importance of shale composition and pore structure upon gas storage potential of shale gas reservoirs. Mar. Petrol. Geol. 26, 916–927.
Sakurovs, R., Day, S., Weir, S., Duffy, G., 2007. Application of a modified Dubinin−Radushkevich equation to adsorption of gases by coals under supercritical conditions. Energy Fuel. 21, 992–997.
Shen, W., Li, X., Cihan, A., Lu, X., Liu, X., 2019. Experimental and numerical simulation of water adsorption and diffusion in shale gas reservoir rocks. Adv. Geo-Energy Res. 3, 165–174.
Shen, W., Li, X., Ma, T., Cai, J., Lu, X., Zhou, S., 2021. High-pressure methane adsorption behavior on deep shales: experiments and modeling. Phys. Fluids 33, 063103.
Shen, W., Ma, T., Li, X., Sun, B., Hu, Y., Xu, J., 2022. Fully coupled modeling of two-phase fluid flow and geomechanics in ultra-deep natural gas reservoirs. Phys. Fluids 34, 043101.
Song, X., Lü, X., Shen, Y., Guo, S., Guan, Y., 2018. A modified supercritical Dubinin–Radushkevich model for the accurate estimation of high pressure methane adsorption on shales. Int. J. Coal Geol. 193, 1–15.
Tang, S., Zhang, J., Elsworth, D., Tang, X., Li, Z., Du, X., Yang, X., 2016. Lithofacies and pore characterization of the lower permian shanxi and taiyuan shales in the southern North China Basin. J. Nat. Gas Sci. Eng. 36, 644–661.
Tang, X., Ripepi, N., Rigby, S., Mokaya, R., Gilliland, E., 2019. New perspectives on supercritical methane adsorption in shales and associated thermodynamics. J. Ind. Eng. Chem. 78, 186–197.
Teng, J., Liu, B., Mastalerz, M., Schieber, J., 2022. Origin of organic matter and organic pores in the overmature ordovician-silurian wufeng-longmaxi shale of the Sichuan Basin, China. Int. J. Coal Geol. 253, 103970.
Tripathy, A., Kumar, A., Srinivasan, V., Singh, K.H., Singh, T.N., 2019. Fractal analysis and spatial disposition of porosity in major indian gas shales using low-pressure nitrogen adsorption and advanced image segmentation. J. Nat. Gas Sci. Eng. 72, 103009.
Vishal, V., Chandra, D., Bahadur, J., Sen, D., Hazra, B., Mahanta, B., Mani, D., 2019. Interpreting pore dimensions in gas shales using a combination of SEM imaging, small-angle neutron scattering, and low-pressure gas adsorption. Energy Fuel. 33, 4835–4848.
Wang, L., Yu, Q., 2016. The effect of moisture on the methane adsorption capacity of shales: a study case in the eastern Qaidam Basin in China. J. Hydrol. 542, 487–505.
Wang, Y., Zhu, Y., Liu, S., Zhang, R., 2016a. Methane adsorption measurements and modeling for organic-rich marine shale samples. Fuel 172, 301–309.
Wang, Y., Zhu, Y., Liu, S., Zhang, R., 2016b. Pore characterization and its impact on methane adsorption capacity for organic-rich marine shales. Fuel 181, 227–237.
Wang, P., Jiang, Z., Yin, L., Chen, L., Li, Z., Zhang, C., Li, T., Huang, P., 2017. Lithofacies classification and its effect on pore structure of the Cambrian marine shale in the Upper Yangtze Platform, South China: evidence from FE-SEM and gas adsorption analysis. J. Petrol. Sci. Eng. 156, 307–321.
Wang, T., Tian, S., Li, G., Sheng, M., Ren, W., Liu, Q., Tan, Y., Zhang, P., 2019. Experimental study of water vapor adsorption behaviors on shale. Fuel 248, 168–177.
Wei, L., Haiyong, Y., Wangshui, H., Geng, Y., Xuan, X., 2014. Tectonic evolution of caledonian palaeohigh in the Sichuan Basin and its relationship with hydrocarbon accumulation. Nat. Gas. Ind. B 1, 58–65.

Wei, M., Zhang, L., Xiong, Y., Li, J., Peng, P., 2016. Nanopore structure characterization for organic-rich shale using the non-local-density functional theory by a combination of N2 and CO2 adsorption. Microporous Mesoporous Mater. 227, 88–94.
Wu, S., Tang, D., Li, S., Chen, H., Wu, H., 2016. Coalbed methane adsorption behavior and its energy variation features under supercritical pressure and temperature conditions. J. Petrol. Sci. Eng. 146, 726–734.
Xiao, B., Liu, S., Li, Z., Ran, B., Ye, Y., Yang, D., Li, J., 2021. Geochemical characteristics of marine shale in the Wufeng Formation–Longmaxi Formation in the northern Sichuan Basin, South China and its implications for depositional controls on organic matter. J. Petrol. Sci. Eng. 203, 108618.
Xiong, F., Rother, G., Tomasko, D., Pang, W., Moortgat, J., 2020. On the pressure and temperature dependence of adsorption densities and other thermodynamic properties in gas shales. Chem. Eng. J. 395, 124989.
Xu, S., Gou, Q., Hao, F., Zhang, B., Shu, Z., Lu, Y., Wang, Y., 2020a. Shale pore structure characteristics of the high and low productivity wells, Jiaoshiba shale gas field, Sichuan Basin, China: dominated by lithofacies or preservation condition? Mar. Petrol. Geol. 114, 104211.
Xu, S., Gou, Q., Hao, F., Zhang, B., Shu, Z., Zhang, Y., 2020b. Multiscale faults and fractures characterization and their effects on shale gas accumulation in the Jiaoshiba area, Sichuan Basin, China. J. Petrol. Sci. Eng. 189, 107026.
Yang, F., Ning, Z., Zhang, R., Zhao, H., Krooss, B.M., 2015. Investigations on the methane sorption capacity of marine shales from Sichuan Basin, China. Int. J. Coal Geol. 146, 104–117.
Yang, F., Ning, Z., Wang, Q., Zhang, R., Krooss, B.M., 2016. Pore structure characteristics of lower Silurian shales in the southern Sichuan Basin, China: insights to pore development and gas storage mechanism. Int. J. Coal Geol. 156, 12–24.
Yang, R., He, S., Yi, J., Hu, Q., 2016. Nano-scale pore structure and fractal dimension of organic-rich Wufeng-Longmaxi shale from Jiaoshiba area, Sichuan Basin: investigations using FE-SEM, gas adsorption and helium pycnometry. Mar. Petrol. Geol. 70, 27–45.
Yang, F., Xie, C., Ning, Z., Krooss, B.M., 2017a. High-pressure methane sorption on dry and moisture-equilibrated shales. Energy Fuel. 31, 482–492.
Yang, F., Xie, C., Xu, S., Ning, Z., Krooss, B.M., 2017b. Supercritical methane sorption on organic-rich shales over a wide temperature range. Energy Fuel. 31, 13427–13438.
Yang, F., Xu, S., Hao, F., Hu, B., Zhang, B., Shu, Z., Long, S., 2019. Petrophysical characteristics of shales with different lithofacies in Jiaoshiba area, Sichuan Basin, China: implications for shale gas accumulation mechanism. Mar. Petrol. Geol. 109, 394–407.
Yang, R., Jia, A., He, S., Hu, Q., Dong, T., Hou, Y., Yan, J., 2020. Water adsorption characteristics of organic-rich Wufeng and longmaxi shales, Sichuan Basin (China). J. Petrol. Sci. Eng. 193, 107387.
Yuan, W., Pan, Z., Li, X., Yang, Y., Zhao, C., Connell, L.D., Li, S., He, J., 2014. Experimental study and modelling of methane adsorption and diffusion in shale. Fuel 117, 509–519.
Zhang, T., Ellis, G.S., Ruppel, S.C., Milliken, K., Yang, R., 2012. Effect of organic-matter type and thermal maturity on methane adsorption in shale-gas systems. Org. Geochem. 47, 120–131.
Zhang, P., Lu, S., Li, J., Zhang, J., Xue, H., Chen, C., 2017. Comparisons of SEM, low-field NMR, and mercury intrusion capillary pressure in characterization of the pore size distribution of lacustrine shale: a case study on the dongying depression, bohai bay basin, China. Energy Fuel. 31, 9232–9239.
Zhang, L., Lu, S., Jiang, S., Xiao, D., Chen, L., Liu, Y., Zhang, Y., Li, B., Gong, C., 2018. Effect of shale lithofacies on pore structure of the wufeng–longmaxi shale in southeast chongqing, China. Energy Fuel. 32, 6603–6618.
Zhang, L., Xiao, D., Lu, S., Jiang, S., Wu, L., 2020. Pore development of the lower longmaxi shale in the southeastern sichuan basin and its adjacent areas: insights from lithofacies identification and organic matter. Mar. Petrol. Geol. 122 (2), 104662.
Zhao, J., Jin, Zhijun, Jin, Zhenkui, Wen, X., Geng, Y., Yan, C., Nie, H., 2017. Depositional environment of shale in Wufeng and longmaxi formations, Sichuan Basin. Petroleum Research 2, 209–221.
Zhou, S., Xue, H., Ning, Y., Guo, W., Zhang, Q., 2018. Experimental study of supercritical methane adsorption in Longmaxi shale: insights into the density of adsorbed methane. Fuel 211, 140–148.
Zhou, J., Liu, M., Xian, X., Jiang, Y., Liu, Q., Wang, X., 2019. Measurements and modelling of CH4 and CO2 adsorption behaviors on shales: implication for CO2 enhanced shale gas recovery. Fuel 251, 293–306.
Zou, J., Rezaee, R., Xie, Q., You, L., Liu, K., Saeedi, A., 2018. Investigation of moisture effect on methane adsorption capacity of shale samples. Fuel 232, 323–332.
Zou, J., Rezaee, R., Xie, Q., You, L., 2019. Characterization of the combined effect of high temperature and moisture on methane adsorption in shale gas reservoirs. J. Petrol. Sci. Eng. 182, 106353.